Far-infrared magnetospectroscopy of the hole pocket in bismuth. I. Band-structure effects*†

H. R. Verdún‡ and H. D. Drew
Department of Physics and Astronomy, University of Maryland, College Park, Maryland 20742
(Received 1 October 1975)

Weak cyclotron, spin-flip, and combined resonances associated with the hole pocket of bismuth have been studied in magnetotransmission experiments at far-infrared frequencies in both the Voigt and Faraday configurations. The experiments were done on single-crystal samples at liquid-helium temperatures in magnetic fields up to 140 kG using far-infrared molecular-gas lasers (HCN, H_2O, D_2O). The anisotropy of the spectra was studied with emphasis on the case in which the magnetic field is oriented in the binary plane. The experimental data have been analyzed in terms of a one-band effective Hamiltonian derived by $\vec{P}\cdot\vec{\pi}$ perturbation theory. Since the observed transitions are forbidden in the effective-mass approximation, the effective Hamiltonian was taken to fourth order in $\vec{P}$ and $\vec{\Pi}$. Higher-order terms can be neglected because the kinetic energy of the holes is small compared with the energy gap to the nearest band. Using Golin's calculations of the interband velocity matrix elements as a guide, the parameters of the effective Hamiltonian have been adjusted to give good account of the positions, linewidths, and intensities of the absorption lines. The resulting Hamiltonian is also consistent with the cyclotron masses and spin-splitting factors reported in the literature for the holes in bismuth. In the single-particle approximation the effective Hamiltonian does not account for the sharp fine structure that is observed on the absorption lines. Experiments show that these features are intrinsic effects in undeformed bismuth. They have been interpreted in terms of electron-electron interaction effects. The analysis of these effects will be published separately.

I. INTRODUCTION

The hole pocket in bismuth has not been nearly so well characterized as in the case for the electrons. The reasons for this are presumably the following: (i) interband magneto-optical transitions involving the holes have not been observed, (ii) cyclotron-resonance signals are weaker because of the heavier hole masses and the shorter hole relaxation times, and (iii) the hole dispersion relations are nearly parabolic and ellipsoidal and the departures are not well described in terms of simple models. Indeed in the several attempts to interpret experimental data in terms of the nonparabolicity of the holes by using an effective two-band model, effective energy-gap parameters that range between[1] 66 and[2] 250 MeV have been obtained. On the other hand, high-precision cyclotron-resonance and Shubnikov–de Haas experiments have not shown any departure from an ellipsoidal Fermi surface for the holes.[3]

Recently, Blewitt and Sievers[4] have made a study of Alfvén wave transmission in bismuth in the far infrared in which they observed weak hole cyclotron-resonance absorption although the propagating mode was cyclotron-resonance inactive. They interpreted the occurrence of the lines in terms of small departures of the hole Fermi surface from ellipsoidity and noted that the observed lines were not inconsistent with the crystal symmetry. The discovery of these absorption lines leads to the possibility of a thorough study of the electronic structure for the holes since their oscillator strength, positions, and linewidths will all be sensitive to the details of the band structure of the hole pocket. This paper presents the results of such a study.

In the experiments performed at far-infrared laser frequencies, electric-dipole–induced spin flip and combined resonances have also been observed in addition to the cyclotron harmonics. All of these transitions have been studied as a function of the orientation of the magnetic field in the binary plane of bismuth in both the Faraday and the Voigt configuration. Also some results are presented for other magnetic field orientations.

Since the hole Fermi-surface dimensions are very small compared with the Brillouin-zone dimensions, it is convenient to describe the electronic structure of the holes in terms of $\vec{k}\cdot\vec{p}$ perturbation theory. We have developed a one-band effective Hamiltonian $\mathcal{H}_{\text{eff}}$ for the holes including terms to fourth order in $\vec{P}=\vec{p}+(e/c)\vec{A}$. Starting with the energy gaps and velocity matrix elements ($\vec{\Pi}$) calculated by Golin,[5] we get an estimate of the fourth-order terms which are responsible for the "forbidden" absorption lines. By fitting the observed positions of the weak absorption lines, the parameters of $\mathcal{H}_{\text{eff}}$ are refined, and good agreement with the present experiments and microwave cyclotron-resonance results are found.

Sharp fine-structure features are also observed on the absorption lines which are not accountable in terms of band-structure effects. These features have been interpreted in terms of collective states of the electron-hole pairs produced in the optical absorption.[6] These effects, which are

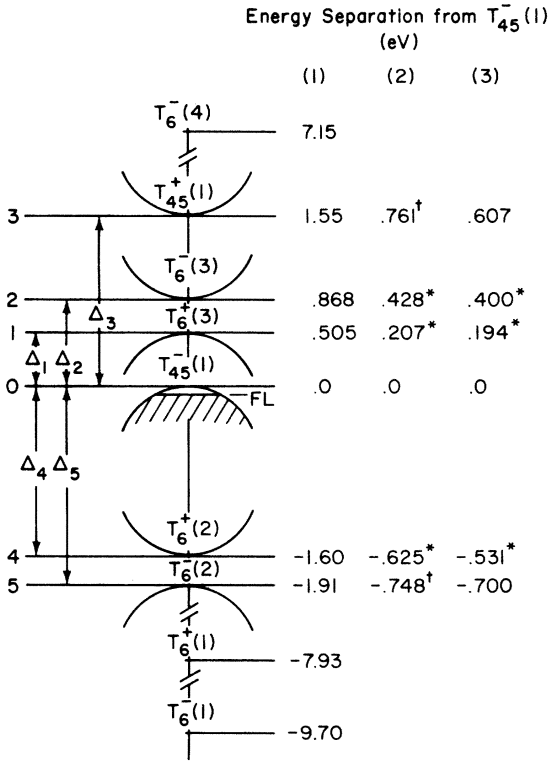

FIG. 1. Bismuth band structure near the T point of the Brillouin zone with the notation and relative positions of the band edges as given by Golin.[5] Column 1 gives Golin's calculated values of the energy gaps. In Col. 2 the values marked with * are "experimental gaps" determined by Golin to adjust experimental hole effective masses and g factor. Values marked with † are the values chosen by Bate *et al.*[13] to fit Shubnikov—de Haas experiments on Sn-doped Bi. Column 3 shows the values that we have chosen. Values marked with * were adjusted to the latest[40] determination of hole effective masses and our own determination of the $\overleftrightarrow{g}^2$.

closely related to the Fermi-liquid effects that have been observed in metals and to excitons in semiconductors, are the subject of a second paper[7] (hereafter referred to as II).

The $\vec{k}\cdot\vec{p}$ ($\vec{P}\cdot\vec{\pi}$ in this case) perturbation theory calculation is presented in Sec. II and the experimental details are described in Sec. III. In Sec. IV we present our experimental results. This is followed by a discussion of the fitting procedure to determine the best parameters for $\mathcal{H}_{eff}$. Concluding remarks and observations are made in Sec. V.

II. ELECTRON BAND THEORY

A. One-band effective Hamiltonian for holes

The one-electron band structure for bismuth has been calculated using the orthogonalized-plane-wave method with relativistic corrections by Ferreira[8] and the pseudopotential method by Golin.[5] These calculations are useful for establishing the main features and spacings of the energy levels at different points in the Brillouin zone. It has been established[9] that the holes in bismuth are located around the T point of the Brillouin zone in one of six closely spaced bands as shown in Fig. 1. The hole Fermi surface is illustrated in Fig. 2. The pseudopotential calculation by Golin is particularly useful because his calculation of the velocity matrix elements needed in $\vec{P}\cdot\vec{\pi}$ perturbation theory calculations appears more reliable.[10]

In the $\vec{P}\cdot\vec{\pi}$ perturbation theory approach the Hamiltonian is effectively expanded in powers of the momentum measured relative to the band extrema point k_0. Using the Luttinger-Kohn representation the eigenfunctions can be written as linear combinations of Bloch functions at k_0 and envelope functions. An effective Hamiltonian can then be found which acts only on these envelope functions and can be used to calculate the energy levels and the transition matrix elements for the optical transitions. We will follow the formalism which is used when a magnetic field is present. This formalism was reviewed by Yafet[11] and more recently by Zeiger and Pratt[12] whose notation we use.

To describe the hole states in bismuth it is necessary to consider the coupling of the six bands near the Fermi level at T which lie within ±2 eV. All other bands lie greater than ~7 eV away. Therefore, a precise treatment of these six Kramer degenerate bands would lead to a 12×12 matrix for the effective Hamiltonian and 12-component wave functions. This approach has been used by Bate *et al.*[13] to account for the nonparabolicity of the hole band observed in Schubnikov-de Haas experiments on bismuth alloys. To study transitions between magnetic states with such a description would be very complicated; however such an approach has been used for the case of InSb.[14]

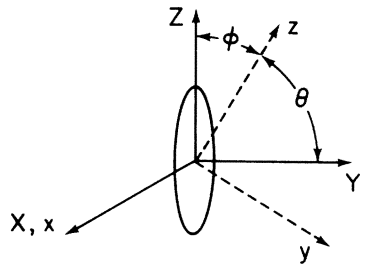

FIG. 2. The Fermi surface for the bismuth holes with the coordinate systems and angle notations used in this paper. X, Y, and Z correspond to the binary, bisectrix, and trigonal axes, respectively. z corresponds to the magnetic field orientation.

In bismuth, the nearest band to the $T_{45}^{-}(1)$ band extremum (the one which lies closest to the Fermi level) appears to be about 200 MeV away, and the Fermi energy of the holes (measured relative to the top of the $T_{45}^{-}(1)$ band) varies only between 10 and 25 MeV in the magnetic field range of our experiments. Indeed these conditions are precisely why nonparabolic and nonellipsoidal effects in the hole pocket are so small. It is therefore a reasonable approximation to reduce the six-band effective Hamiltonian to a one-band effective Hamiltonian by the Brillouin-Wigner decoupling scheme.[12] With this reduction the effective Hamiltonian reduced to a 2×2 matrix with two-component "wave functions." Using Brillouin-Wigner perturbation theory the effective Hamiltonian for the band j (T_{45}^{-} in our case) can be written[12]

$$(\mathcal{H}_{\text{eff}})_{jj} = \mathcal{E}_j^{(0)} + \frac{\vec{P}^2}{2m_0} + \sum_{\mu} \frac{\mathcal{H}_{1j\mu}\mathcal{H}_{1\mu j}}{(\mathcal{E}-\mathcal{E}_\mu^{(0)})} + \sum_{\mu\nu} \frac{\mathcal{H}_{1j\mu}\mathcal{H}_{1\mu\nu}\mathcal{H}_{1\nu j}}{(\mathcal{E}-\mathcal{E}_\mu^{(0)})(\mathcal{E}-\mathcal{E}_\nu^{(0)})} + \sum_{\mu\nu\eta} \frac{\mathcal{H}_{1j\mu}\mathcal{H}_{1\mu\nu}\mathcal{H}_{1\nu\eta}\mathcal{H}_{1\eta j}}{(\mathcal{E}-\mathcal{E}_\mu^{(0)})(\mathcal{E}-\mathcal{E}_\nu^{(0)})(\mathcal{E}-\mathcal{E}_\eta^{(0)})} + \cdots , \quad (1)$$

where

$$\mathcal{H}_{1nn'} = \vec{\Pi}_{nn'}\cdot\vec{P} + (\vec{P}^2/2m_0)\delta_{nn'} + 2\mu_0 \vec{S}_{nn'}\cdot\vec{H} , \quad (2)$$

and in this expression $\vec{P} = \vec{p} + (e/c)\vec{A}$ and $\vec{\Pi}_{nn'}$ and $\vec{S}_{nn'}$ are the velocity and spin matrix elements defined in Ref. 12.

The momentum $\vec{P}$ is measured relative to the T point and $\mathcal{E}_n^{(0)}$ is the energy of an electronic state at the T point in band n. We have used Golin's results for the matrix elements of $\vec{\Pi}$, and the matrix elements of $\vec{S}$ can be neglected in Eq. (2) in comparison with the other terms.

Following standard procedures[12] the one-band effective Hamiltonian to fourth order in $\vec{P}$ and $\vec{\Pi}$ becomes

$$(\mathcal{H}_{\text{eff}})_{jj} = \mathcal{E}_j^{(0)} + \frac{\vec{P}^2}{2m_0} + \sum_{\mu} \frac{\vec{P}\cdot\vec{\Pi}_{j\mu}\vec{\Pi}_{\mu j}\cdot\vec{P}}{(\mathcal{E}_j^{(0)}-\mathcal{E}_\mu^{(0)})} - \left[\sum_{\mu} \frac{\vec{P}\cdot\vec{\Pi}_{j\mu}\vec{\Pi}_{\mu j}\cdot\vec{P}}{(\mathcal{E}_j^{(0)}-\mathcal{E}_\mu^{(0)})^2} , \left(\frac{P^2}{2m_0}\sum_{\nu} \frac{\vec{P}\cdot\vec{\Pi}_{j\nu}\vec{\Pi}_{\nu j}\cdot\vec{P}}{(\mathcal{E}_j^{(0)}-\mathcal{E}_\nu^{(0)})}\right)\right]_S + \sum_{\mu} \frac{\vec{P}\cdot\vec{\Pi}_{j\mu}(\vec{P}^2/2m_0)\vec{P}\cdot\vec{\Pi}_{\mu j}}{(\mathcal{E}_j^{(0)}-\mathcal{E}_\mu^{(0)})^2} + \sum_{\mu\nu\eta} \frac{\vec{P}\cdot\vec{\Pi}_{j\mu}\vec{P}\cdot\vec{\Pi}_{\mu\nu}\vec{P}\cdot\vec{\Pi}_{\nu\eta}\vec{P}\cdot\vec{\Pi}_{\eta j}}{(\mathcal{E}_j^{(0)}-\mathcal{E}_\mu^{(0)})(\mathcal{E}_j^{(0)}-\mathcal{E}_\nu^{(0)})(\mathcal{E}_j^{(0)}-\mathcal{E}_\eta^{(0)})} , \quad (3)$$

where $[A, B]_S = \frac{1}{2}(AB+BA)$. This can be rewritten

$$\mathcal{H} = \mathcal{H}_1 + \mathcal{H}_2 = (\mathcal{H}_{\text{eff}})_{jj} , \quad (3a)$$

$$\mathcal{H}_1 = \frac{1}{2m_0}\vec{P}\cdot\vec{\alpha}\cdot\vec{P} + \mu_0(G_1\sigma_1 + G_2\sigma_2)H_z , \quad (3b)$$

$$\mathcal{H}_2 = \frac{1}{m_0^2}[A(\{P_X^4 + P_Y^4\} + \tfrac{1}{3}\{P_X P_X P_Y P_Y\}) + B(\{P_X P_X P_Y P_Z\} - \{P_Y P_Y P_Y P_Z\}) + C(\{P_X P_X P_Z P_Z\} + \{P_Y P_Y P_Z P_Z\}) + DP_Z^4] + \frac{\mu_0}{m_0}\sum_{\substack{\alpha,\beta \\ i,j}} \sigma_\alpha H_\beta G_{\alpha\beta,ij}\{P_i P_j\} + \mu_0^2[Q_\perp(H_X^2 + H_Y^2) + Q_\parallel H_Z^2] . \quad (3c)$$

In the above expression $[AB\cdots]$ means the sum of all possible and different permutations of A, B, ..., and the σ_α are the Pauli spin matrices. Using the energy gaps indicated in Fig. 1 and Golin's matrix elements, we have calculated the coefficients involved in (3c). The results are presented in Table I.

With these energy gaps we can estimate the magnitude of the fourth-order correction terms ($\mathcal{H}_2$). From Eq. (3) it is seen that these higher-order terms are smaller than the second-order terms by a factor of order $|\vec{P}\cdot\vec{\Pi}/E_{\text{gap}}|^2$ where E_{gap} should be the smallest energy gap Δ_1. This part of the Hamiltonian will contribute corrections to the parabolic dispersion relations of order

$$\frac{\langle|\vec{P}\cdot\vec{\Pi}|^2\rangle}{E_{\text{gap}}^2} \sim \frac{m_{\text{eff}}}{m_0}\frac{E_F}{E_{\text{gap}}} \sim \frac{1}{10} .$$

Similar arguments indicate that the sixth-order terms would produce a ~1% correction so that stopping at the fourth-order terms in $\mathcal{H}_{\text{eff}}$ is a reasonable approximation.

The calculated parameters present a starting point for the determination of the best effective Hamiltonian for the holes. On the other hand Eq. (3) represents the general form of the effective Hamiltonian for the holes in bismuth to fourth order in P, and as such it provides a convenient

TABLE I. Parameters for the effective Hamiltonian (4a)–(4c) and expressions (6c)–(10) (cgs. units)*.[a]

Parameter	From Golin's velocity matrix elements[b]	Chosen to fit experiments
$\alpha_{XX}=\alpha_{XY}$	15.87	16.87
α_{ZZ}	1.529	1.626
G_1	−39.6	−39.6
G_2	−55.6	−55.6
A	−3.64	−1.82
B	−0.221	−0.110
C	−0.0669	−0.0334
D	−0.0156	−0.0078
$Q_{\parallel}$	−3.04	...
$Q_{\perp}$	15.4	...
$G_{11,12}=G_{11,21}$	1.67	0.67
$G_{11,13}=G_{11,31}$	0.702	0.28
$G_{12,11}=G_{12,22}$	1.67	0.67
$G_{12,23}=G_{12,32}$	0.702	0.28
$G_{13,11}=G_{13,22}$	16.25	6.5
$G_{13,33}$	−0.001	−0.00041
$G_{21,12}=G_{21,21}$	− .93	−0.37
$G_{21,13}=G_{21,31}$	.24	0.095
$G_{22,11}=G_{22,22}$	−0.93	−0.37
$G_{22,23}=G_{22,32}$	0.24	0.095
$G_{23,11}=G_{23,22}$	12.8	5.1
$G_{23,33}$	0.93	0.37
$G_{31,11}=G_{31,22}$	−1.90	−0.76
$G_{31,13}=G_{31,31}$	−0.10	−0.04
$G_{32,12}=G_{32,21}$	1.90	0.76
$G_{32,23}=G_{32,32}$	−0.10	−0.04
$G_{33,11}=G_{33,22}$	0.20	0.08
$a=0.5811\times\mathrm{sgn}(\theta)$		$b=0.8139\times\mathrm{sgn}(\theta)$
$\lambda_1^s=-as$,	$\lambda_2^s=-bs$,	$\lambda_3^s=0$

[a]Coefficients A, B, C, D, $Q_{\parallel}$, $Q_{\perp}$ and the elements of the tensor $G_{\alpha\beta,ij}$ are given in units of 10^{14}.

[b]Energy gaps used in the calculation were those shown in Col. (3) of Fig. 1.

parametrization in which to fit the experimental resonance positions, widths, and oscillator strengths.

B. Hole dispersion relations

Regarding $\mathcal{H}_2$ as a perturbation of $\mathcal{H}_1$ ($\langle\mathcal{H}_2\rangle/\langle\mathcal{H}_1\rangle\sim\frac{1}{10}$) under conditions for which any two levels of $\mathcal{H}_1$ coupled by $\mathcal{H}_2$ do not come too close together, the eigenvalues of $\mathcal{H}$ can be found by first-order nondegenerate perturbation theory. In the remainder of the paper the sign of the energy and the sign of the electron charge will be changed to correspond to hole states instead of electron states. Also, we will measure energies from the top of the $T_{45}^{-}(1)$ band.

For the case in which $\mathcal{H}$ is on the binary plane (corresponding to the experiments) we have for the eigenvalues and eigenfunctions of $\mathcal{H}_1$

$$\mathcal{E}_{n,k_z,s}=(n+\tfrac{1}{2}+\tfrac{1}{2}s\gamma)\hbar\omega_c+\frac{k_z^2}{2m_0}\alpha_H\ , \tag{4}$$

$$\psi_{n,k_z,\sigma}=\frac{1}{L}\,e^{i(k_y y+k_z z)}\,\varphi_n\left\{\left(\frac{m_0\omega_c}{\hbar\alpha_1}\right)^{1/2}\times\left[x-l_0^2\left(k_y+\frac{\alpha_4}{\alpha_2}k_z\right)\right]\right\}|s\rangle\ , \tag{5a}$$

$$\varphi_n(x)=2^{-n/2}\pi^{-1/4}(n!)^{-1/2}e^{-x^2/2}H_n(x)\ , \tag{5b}$$

$$|s\rangle=\frac{1}{\sqrt{2}}\begin{pmatrix}s\,\dfrac{G_1+iG_2}{(G_1^2+G_2^2)^{1/2}}\\ 1\end{pmatrix}\ ,\quad s=\pm1\ , \tag{5c}$$

where

$$\omega_c=(\alpha_1\alpha_2)^{1/2}\omega_{c0}\ ,\quad l^2=l_0^2(\alpha_1/\alpha_2)^{1/2}\ ,\quad l_0^2=\hbar c/eH\ , \tag{5d}$$

$$\gamma=\tfrac{1}{2}[(G_1^2+G_2^2)/(\alpha_1\alpha_2)]^{1/2}\cos\phi\ , \tag{5e}$$

$$\alpha_H=\alpha_3-\alpha_4^2/\alpha_2\ , \tag{5f}$$

and

$$\begin{aligned}&\alpha_1=\beta_1\ ,\\ &\alpha_2=\beta_1\sin^2\theta+\beta_3\cos^2\theta\ ,\\ &\alpha_3=\beta_1\cos^2\theta+\beta_3\sin^2\theta\ ,\\ &\alpha_4=(\beta_1-\beta_3)\sin\theta\cos\theta\ .\end{aligned} \tag{5g}$$

We are introducing here the following definitions:

$$\beta_1=\beta_2\equiv\alpha_{XX}=\alpha_{YY}\equiv1/M_1=1/M_2\ ,\quad \beta_3\equiv\alpha_{ZZ}\equiv1/M_3\ .$$

The $H_n(x)$ are the Hermetian polynomials.

The first-order perturbation theory correction to the part of the energy which is spin independent (the orbital part) produced by $\mathcal{H}_2$ is

$$\delta\mathcal{E}_{n,k_z}^{\mathrm{orb}}=\mathfrak{A}(\hbar\omega_c)^2(n^2+n+\tfrac{1}{2})+\mathfrak{B}\hbar\omega_c(n+\tfrac{1}{2})p_z^2/m_0+\mathfrak{C}p_z^4/m_0^2\ , \tag{6a}$$

$$\mathfrak{A}=A\left(\frac{3}{2}\,\frac{1}{\alpha_1^2}+\frac{\cos^2\phi}{\alpha_1\alpha_2}+\frac{3}{2}\,\frac{\cos^4\phi}{\alpha_2^2}\right)-\frac{3B}{\alpha_1\alpha_2}\sin2\phi\left(1-\frac{\alpha_1}{\alpha_2}\cos^2\phi\right)+\frac{3C}{\alpha_1\alpha_2}\sin^2\phi(1+\cos^2\phi)+\tfrac{3}{2}D\,\frac{\sin^4\phi}{\alpha_2^2}\ , \tag{6b}$$

$$\mathfrak{B}=\frac{3A}{\alpha_1}u^2\left(1+2\,\frac{\beta_2}{\alpha_2}\cos^2\phi\right)+12B\sin2\phi\sin^2\phi\,\frac{\beta_3^2}{\alpha_2^3}+\frac{6C}{\alpha_2}(1-3uv\sin2\phi)+\frac{6D}{\alpha_2}v^2\sin^2\phi\ , \tag{6c}$$

$$\mathfrak{C}=Au^4-4Bu^3v+6Cu^2v^2+Dv^4\ . \tag{6d}$$

In these expressions u and v are given by

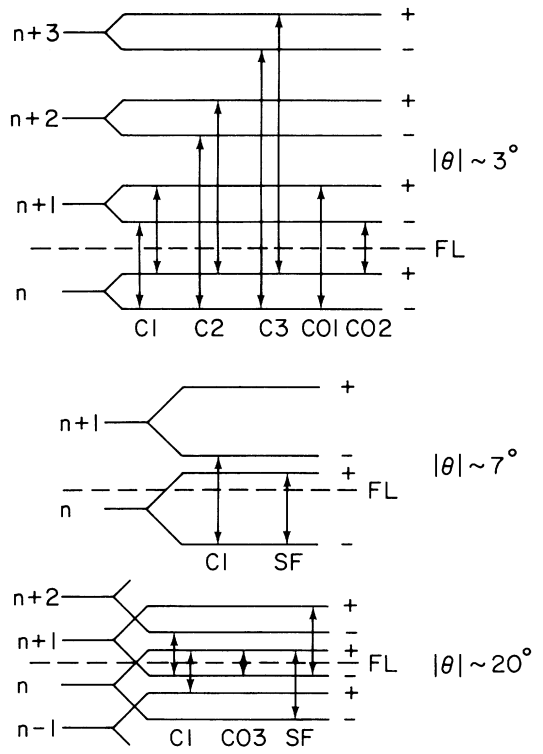

FIG. 3. Optical transitions in the hole pocket allowed by the effective Hamiltonian taken to fourth order in $\vec{P}\cdot\vec{\pi}$ perturbation theory. C1, C2, and C3 are the fundamental and the second and third harmonics of cyclotron resonance. SF is a spin-flip transition and CO1, CO2, and CO3 denote the different kinds of combined resonances.

$$u = \beta_2 \sin\phi/(\beta_2\cos^2\phi + \beta_3\sin^2\phi)\,, \tag{7a}$$

$$v = \beta_2 \cos\phi/(\beta_2\cos^2\phi + \beta_3\sin^2\phi)\,. \tag{7b}$$

For the spin-dependent part the correction term is

$$\delta\mathcal{E}^{\rm spin}_{n,k_z,s} = \left(\frac{\mathcal{G}^s_{xx}}{\alpha_1} + \frac{\mathcal{G}^s_{yy}}{\alpha_2}\right)(n+\tfrac{1}{2})\hbar\omega_c + \left[\mathcal{G}^s_{zz} - 2\mathcal{G}^s_{yz}\frac{\alpha_4}{\alpha_2} + \mathcal{G}^s_{yy}\left(\frac{\alpha_4}{\alpha_2}\right)^2\right]\frac{p_z^2}{m_0}\,, \tag{8a}$$

$$\mathcal{G}^s_{ij} = \mu_0 \sum_{\alpha,\beta} \overleftrightarrow{G}_{\alpha\beta,ij}\lambda^s_\alpha H_\beta\,, \tag{8b}$$

$$\lambda^s_\alpha = \langle s|\sigma_\alpha|s\rangle\,, \tag{8c}$$

where $\overleftrightarrow{G}_{\alpha\beta,ij}$ is the tensor obtained from $G_{\alpha\beta,ij}$ when we represent $\vec{P}_i$ in the x, y, z coordinate system. Table I gives the values of λ^s_α.

For $H=0$, the effective Hamiltonian reduces to

$$\mathcal{H} = \frac{1}{2m_0}\vec{P}\cdot\overleftrightarrow{\alpha}\cdot\vec{P} + \frac{1}{m_0^2}[Ap_\perp^4 + 4Bp_\parallel p_\perp^3\sin(3\Phi) + 6Cp_\perp^2p_\parallel^2 + Dp_\parallel^4]\,, \tag{9}$$

where $\vec{p}_\perp = \vec{p}_X\hat{X} + \vec{p}_Y\hat{Y}$, $p_\parallel = \vec{p}_Z$, and Φ is the angle between $\vec{p}_\perp$ and $\hat{Y}$. The eigenvalues of this Hamiltonian are given by an expression similar to that derived by Bate *et al.*[13] except that their coefficients are functions of the energy while A, B, C, and D are constants in our approach.

C. Matrix elements and optical absorption

The effective Hamiltonian Eq. (3) can be used to calculate transition matrix elements for different kinds of transitions by the method described by Zeiger and Pratt.[12] For the long-wavelength propagating magnetoplasma waves in our experiments we can neglect the spatial dispersion of the time varying electromagnetic field (the dipole approximation). The matrix elements are then calculated from

$$M_{fi} = \langle f|\mathcal{H}'|i\rangle\,, \tag{10}$$

where $\mathcal{H}'$ is the time-dependent part of the Hamiltonian obtained by taking the vector potential to be $\vec{A}+\vec{A}'(t)$ where

$$A'(t) = \tfrac{1}{2}[-(c/i\omega)\vec{E} + e^{i\omega t} + \text{c.c.}]$$

and keeping only terms linear in $\vec{E}$.

It is consistent with the perturbational approach we are adopting to take the wave functions for the effective Hamiltonian obtained by first-order perturbation theory,

$$|\bar{\rho}\rangle = |\rho\rangle + \sum_{\rho'}\frac{\langle\rho'|\mathcal{H}_2|\rho\rangle}{E_\rho - E_{\rho'}}|\rho'\rangle\delta_{k_z,k_z'}\delta_{k_y,k_y'}\,, \tag{11}$$

where ρ and ρ' stand for $(n,\ k_y,\ k_z,\ s)$ and $(n',\ k_y',\ k_z',\ s')$, respectively. The zero-order wave functions will be taken to be normalized to 1, so that we are ignoring the normalization condition for the envelope functions.[12,15] This approximation introduces an error of order $E_F/E_g \sim \frac{1}{10}$ which is unimportant to our aim of getting an order-of-magnitude estimate of the absorption.

The time-dependent Hamiltonian has terms coming from both $\mathcal{H}_1$ and $\mathcal{H}_2$. To get a first-order result in the coefficients A, B, D, and $G_{\alpha\beta,ij}$ we must consider both the transition matrix elements corresponding to $\mathcal{H}_1'$, taken between the envelope functions including first-order corrections and keeping terms of first order in those coefficients, and the transition matrix elements of $\mathcal{H}_2'$ taken between zero-order envelope functions. This procedure is equivalent to the one used by Rashba and Sheka.[16] Therefore, the matrix element becomes

$$\langle^-|\mathcal{H}'|^-\rangle = \langle^-|\mathcal{H}_1'|\rangle + \langle|\mathcal{H}_1'|^-\rangle + \langle|\mathcal{H}_2'|\rangle\,. \tag{12}$$

The transitions allowed by $\mathcal{H}_{\rm eff}$ are shown in Fig. 3. The corresponding transition matrix elements are given in the Appendix. We note here that the magnetic dipole transitions and transi-

TABLE II. Far-infrared Laser lines used in the experiments.

Wavelength (μm)	Frequency (GHz)	Molecular-gas laser
118.591[a]	2527.9	H_2O
171.67[a]	1746.3	D_2O
311.08[b]	963.7	HCN
336.85[b]	889.9	HCN

[a]Reference 41. [b]Reference 42.

tions induced by the effective spin-orbit interaction considered by Wolff[17] for the electrons have also been examined, but their contributions are small compared with the transitions corresponding to Eq. (12).

The "forbidden" transitions permitted by $\mathcal{H}_2$ are typically orders of magnitude weaker than the "allowed" transitions from $\mathcal{H}_1$. We can therefore neglect the contributions of these weak transitions to the real part of the dielectric function in calculating the absorption. The transition rate calculated from the Fermi golden rule is then

$$W_{fi}(\omega) = \frac{2\pi}{\hbar} \sum_{\rho'\rho} |M_{fi}(\rho', \rho)|^2 [f(\mathcal{E}_\rho) - f(\mathcal{E}_{\rho'})] \times \mathfrak{D}(\mathcal{E}_{\rho'} - \mathcal{E}_\rho - \hbar\omega) \delta_{k_y', k_y + q_y} \delta_{k_z', k_z + q_z}, \quad (13)$$

where ρ and ρ' stand for (n, k_y, k_z, s) and (n', k_y', k_z', s'), respectively, and $f(\mathcal{E})$ is the Fermi-Dirac distribution function.

Scattering processes will be accounted for only in the relaxation time approximation by writing

$$\mathfrak{D}(\mathcal{E}) = \frac{\delta/\pi}{\mathcal{E}^2 + \delta^2}, \quad (14)$$

taking δ constant and defining a relaxation time by $\delta = \hbar/\tau$.

The absorption coefficient is then given by

$$\alpha(\omega) = \hbar\omega \, W_{fi}(\omega)/\underline{P}, \quad (15)$$

where $\underline{P}$ is the modulus of the time-average Pointing vector. $\underline{P} = (c^2 8/8\pi\omega)(|E_x|^2 + |E_y|^2)$ for the Faraday configuration and $\underline{P} = (c^2 8/8\pi\omega)|E_y|^2$ for the Voigt configuration.

III. EXPERIMENTAL DETAILS

A. Far-infrared magneto-optical spectroscopy

Most of the experiments were done using monochromatic far-infrared radiation produced by molecular-gas lasers pumped by an electrical discharge. The available frequencies are listed in Table II. The lasers are of conventional design consisting of Fabry-Perot cavities with one flat and one spherical mirror whose radius is somewhat larger than the mirror separation. The electrodes are made of copper and are in the shape of hollow cylinders. Invar rods are used to maintain constant mirror separation in spite of the thermal expansion of the glass cavity. The dimensions of the H_2O laser are as follows: laser tube diameter, 10 cm; mirror separation, 5.4 m; mirror radius, 10 m; electrode separation, 4.9 m. The far-infrared radiation is coupled out through a 2–3-mm-diam hole in the center of the fixed flat mirror. The output is of the order of milliwatts for 118-μm radiation and the short-term stability is typically 0.1% for a 1-Hz bandwidth.

The experimental arrangement for the different sample configurations of interest are shown in Fig. 4. The radiation was channeled to the sample and detector using $\frac{1}{2}$-in. brass and stainless-steel light pipe optics. The far-infrared detector was a 4.2 °K Ga-doped Ge bolometer which has been described elsewhere.[18]

The room temperature window was a 0.5-mm polyethylene disk. The low-temperature window of the Faraday configuration cryostat was made with a quartz disk with O-ring vacuum seal so that the detector chamber could be kept under vacuum conditions. To produce thermal contact of the sample to the liquid-He bath, a small amount of ^{4}He exchange gas was admitted to the sample compartment. To minimize thermal leak from room temperature the light pipe inside the cryostats was

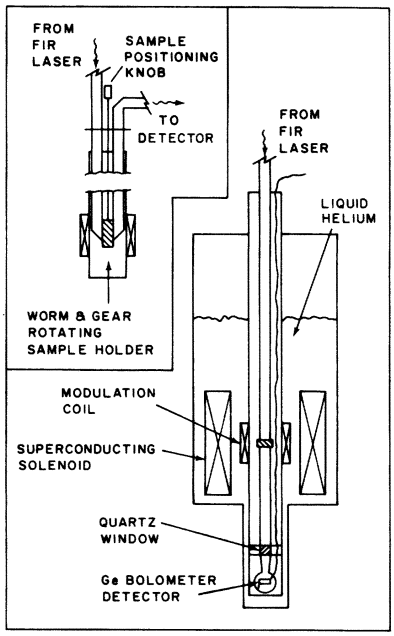

FIG. 4. Schematic representation of the experimental arrangement and the cryostate design. The inset shows details of the rotating sample holder for the Voigt configuration.

made from thin-wall stainless-steel tubing.

The sample was held lightly up against the lower end of the light pipe with a berylium-copper spring. Attached to the sample holder was a carbon resistor for temperature measurement and a heater. These two elements were used in a regulation loop to provide temperature control. The detector chamber was located 13 in. below the superconducting solenoid and surrounded with a lead superconducting shield to avoid magnetic field effects on the FIR detector.

Magnetic fields up to 100 kG were produced by a superconducting solenoid with a bore diameter of 38 mm. The magnetic field was measured by current calibration using a NMR probe and ^{1}H and ^{19}F resonances with a reproducibility better than 0.2% in the range from 15 to 100 kG. The alignment of the magnetic field with the cryostat axis was checked by using the orientation sensitivity of the combined resonance in bismuth near the bisectrix axis (CO1 in Figs. 5 and 8). For orientations where the magnetic field is close to the bisectrix axis and for the 311-μm radiation from the HCN laser the sensitivity is 7.8 kG/deg. By this technique the magnetic field was determined to have a misorientation of no more than 0.5°. The accuracy in the positioning of the sample in the sample holder of the Faraday configuration cryostat was estimated to be better than 0.1°. The magnetic field homogeneity was also checked by NMR and was found to be better than 0.3% in a $\frac{1}{2}$-in. length along the axis at the center of the solenoid.

Magnetic field modulation was available from a coil wound externally around the $1\frac{1}{4}$-in.-diam stainless-steel outer wall of the cryostat at the level of the sample holder. This coil was capable of producing a modulation of 200 G peak to peak with a power dissipation of 0.1 W at $H=0$ and ~0.3 W at 100 kG.

In the Voigt configuration cryostat, the sample holder was constructed to permit 360° rotation of the sample around a horizontal axis. The orientation was controlled by means of a worm-gear arrangement that could be adjusted externally during the experiments. To avoid strain effects, the sample was attached to the rotating holder by glueing it in only a small area (about 2 mm) on its periphery using GE 7031 varnish. The positioning accuracy was to within 0.2°.

Some of the far-infrared measurements were made at the facility for magneto-optical studies at the Naval Research Laboratory in Washington, D. C. In this case many far-infrared (FIR) lines from an optically pumped molecular-gas laser and magnetic fields up to 140 kG produced by a Bitter magnet were available. The characteristics of this facility have been described elsewhere.[19]

B. Sample preparation

The crystals were grown either directly from 0.999999 purity bismuth available commerically or from a zone-refined batch of this material. The zone refining was done following standard procedures.[20] The crystal growing procedure was essentially the same as described by Strom.[21] Only single-crystal samples without twinning planes or other morphological defects were used in the experiments to avoid possible straining effects that could be produced when the crystal was cooled to liquid-helium temperatures. The crystals were spark-cut and spark-planed to the desired size and shape and then etched in a nitric acid solution to remove the damaged layers. Typically 50 μm of material was removed. This etch produced a rough surface which was desirable for reducing the amplitude of the Fabry-Perot interferrometric oscillations in the transmission experiments. The sample orientation was determined to within $\frac{1}{2}$° from back-reflection x-ray Laue patterns using a Cu cathode, and by comparison with the spectra obtained in Voigt configuration using the rotating sample holders.

Resistivity ratio measurements were made on specimens cut from some of our crystals using the four-lead technique. For the zone-refined bismuth the resistivity ratio was typically about 300. Since the specimens had rather small cross sections (~0.5×2 mm) the ratio was limited by the size effect. From the results of Friedman,[22] the bulk ratios are estimated to be about 750 for these samples.

IV. EXPERIMENTAL RESULTS

A. Magnetic field in the binary plane

Typical magnetotransmission spectra for Faraday configuration samples are shown in Fig. 5. The spectrum for the $\theta=-2.1$° sample has examples of many of the features that we will be referring to throughout the remainder of this paper. A sharp transmission edge is seen at about 27 kG. This is the magnetic field for which all of the electron pockets go into the extreme quantum limit, and the increased transmission is thought to arise from a reduction of carrier scattering processes owing to phase-space restrictions in the extreme quantum case. Over most of the high-transmission part of the spectrum a fine oscillatory signal is seen whose period and amplitude increases with magnetic field. These are Fabry-Perot interference fringes of the propagating magnetoplasma waves in the parallel face sample. At 35-, 63-, and 75-kG regions attenuation is seen which is either broad absorption or a collec-

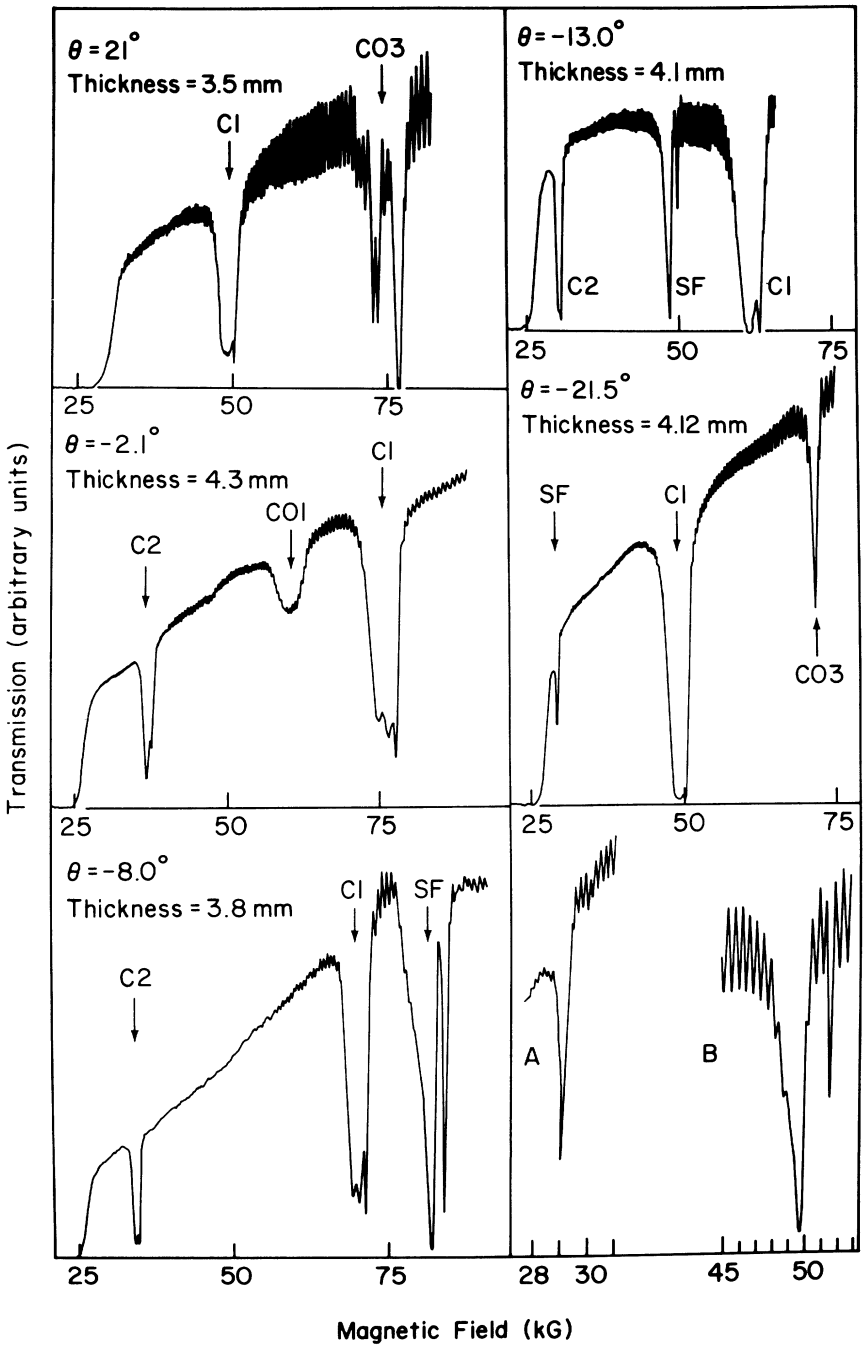

FIG. 5. Magnetotransmission spectra in the Faraday configuration for several different sample orientations at 964 GHz. $T = 4.3\,^{\circ}\mathrm{K}$. A and B are the SF absorption peaks for $\theta = -21.5^{\circ}$ and $\theta = -13^{\circ}$, respectively, in expanded scale. The fine oscillatory signals, particularly noticeable in B, for example, are due to Fabry-Perot interferences in the parallel face samples.

tion of several narrow absorption peaks which, in either case, typically span an interval of about 10% of the magnetic field corresponding to their center of gravity. We will call these features absorption lines, and the narrow component features will be referred to as the fine structure of the absorption line. A series of Faraday geometry spectra for different laser frequencies and different sample orientations are shown in Figs. 5–7. In Fig. 8 we show the orientation dependence Voigt geometry spectra at 337 μm.

In the spectra of Fig. 5 ($\theta = -2.1^{\circ}$) and Fig. 6, or in the spectrum of Fig. 7, it is easy to identify a series of cyclotron-resonance harmonics. This series was first identified by Blewitt and Sievers[4] as cyclotron resonance of the carriers in the hole pocket by comparison with the hole cyclotron masses observed at microwave frequencies. The

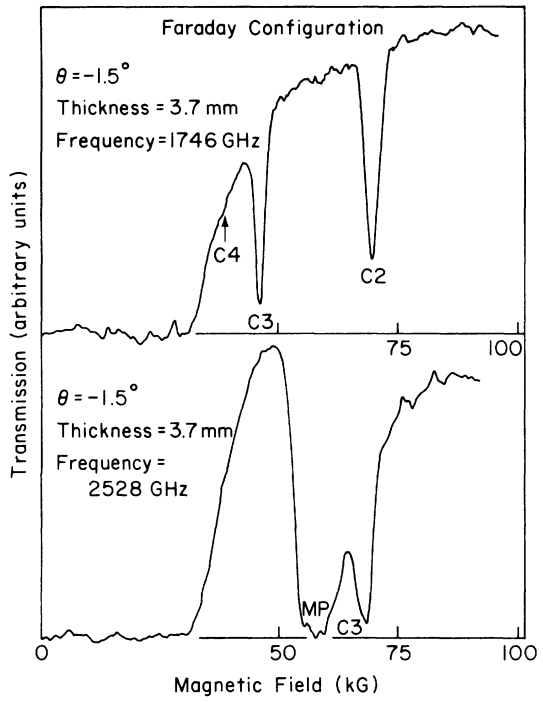

FIG. 6. Magnetotransmission spectra in the Faraday configuration at 1746 GHz and 2528 GHz. $T = 4.3\,^{\circ}\mathrm{K}$.

dependence of the position of the absorption peak that corresponds to the fundamental hole cyclotron resonance with the magnetic field orientation in the binary plane is shown in Fig. 9. This plot contains the experimental results obtained in Voigt configuration (Fig. 8) and the peak position has been marked at the high magnetic field side where there is always a sharp edge or sharp "fine-structure" feature like a narrow peak emerging from a broader structure.

In all these figures of spectra there are several other absorption lines with positions that change rapidly with orientation. The relation between the position of these peaks and the magnetic field orientation on the binary plane is also shown in Fig. 9, again for the Voigt configuration spectra (Fig. 8). The peak positions have been marked in a similar fashion as for the fundamental hole cyclotron resonance (HCR).

The strong and almost symmetric dependence of positions versus the angle θ that the magnetic field makes with the bisectrix axis indicates that these absorption peaks must be related with a very anisotropic property of holes. From previous studies of the hole magnetic levels[23-26] the spin-splitting γ for holes is known to be almost zero for H parallel to the bisectric axis ($\theta = 0°$) and near 2 for H parallel to the trigonal axis ($\theta = \pm 90°$). Clearly, this spin-splitting is a very anisotropic property of the holes, and so it is natural to assume that these absorption peaks are related with transitions involving a spin-flip.

The peaks with positions on curve B of Fig. 8 almost collapse into the fundamental cyclotron-resonance line at $\theta \sim 0$, and so they must correspond to transitions in which the Landau quantum number changes by $+1$. This identifies these lines as combined resonances involving transitions of the type CO1 and CO2 defined in Fig. 3.

From the known dependence of γ upon θ, it is expected that the spin-splitting will be equal to the separation between Landau levels for $|\theta| \sim 10°$ so that the peaks corresponding to curve C of Fig. 9 must be spin-flip resonances. Finally, since γ is larger than 1 for $|\theta| > 10°$, combined resonances involving a change of -1 in the Landau quantum number are possible, and the absorption lines represented by curve D correspond to these kinds of transitions (CO3 transitions Fig. 3). The peak marked MP in Fig. 6 is an example of a magnetoplasma resonance that has been identified by Blewitt and Sievers.[4]

B. Magnetic field in the trigonal plane

The transmission spectra at 311 and 337 μm for H in the trigonal plane are shown in Figs. 10 and 11. The absorption peak marked P2 has also been seen very weakly in some bisectrix samples. This fact suggests that the intensity of this peak

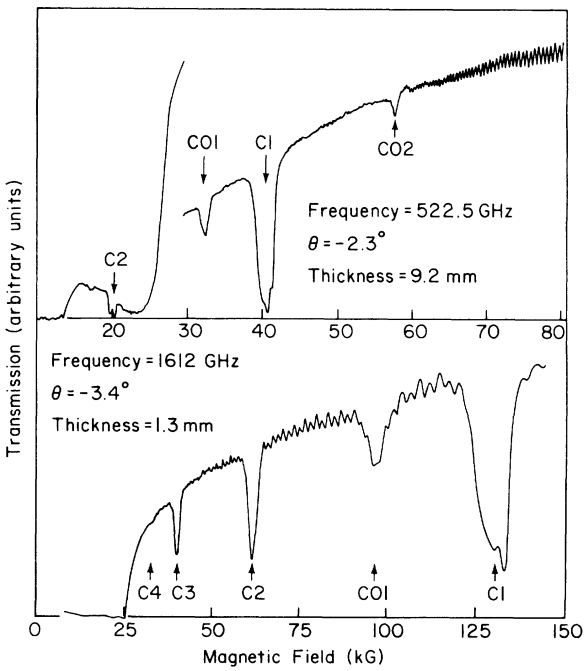

FIG. 7. Magnetotransmission spectra in the Faraday configuration at 522.5 GHz and 1612 GHz. $T = 4.3\,^{\circ}\mathrm{K}$.

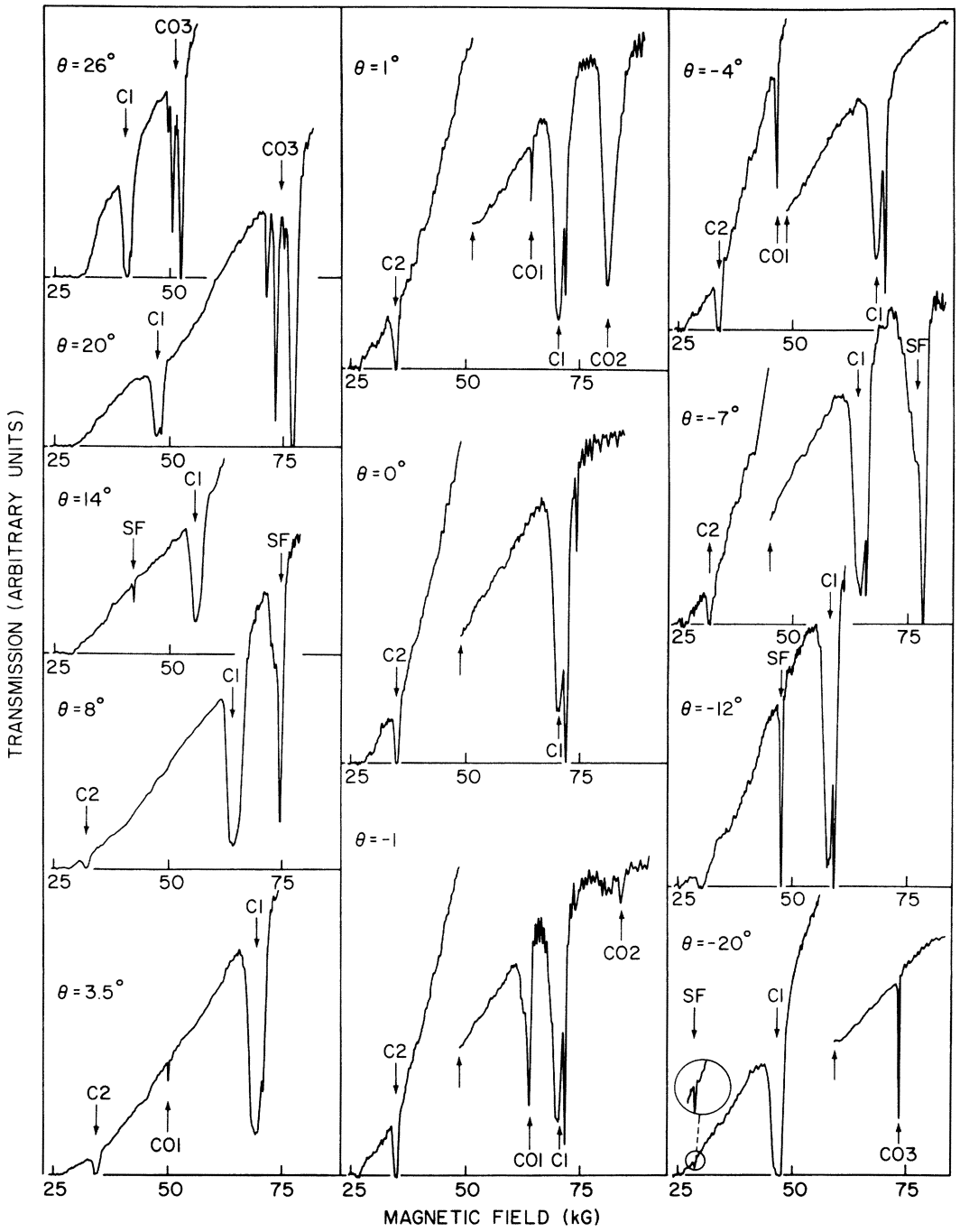

FIG. 8. Magnetotransmission spectra in the Voigt configuration for H in the binary plane. The sample thickness is 3 mm and the frequency is 890 GHz. $T=4.3\,^{\circ}$K. The arrows indicate a change in the vertical scale.

is zero for H parallel to the bisectrix axis and increases when H moves away from this orientation in the trigonal plane. In the spectrum for $\psi=6^{\circ}$, the peaks marked as $C1$, $C2$, and COl look quite similar to the same peaks that we have for H in the binary plane and $\theta=-2.1^{\circ}$, suggesting that for this sample H was about -2° from the trigonal plane.

For H parallel to the binary axis, one electron pocket has a cyclotron mass which is about half the cyclotron mass for holes. This electron pocket produces a strong cyclotron-resonance absorption around 30 kG for 311-μm radiation since the propagating mode corresponds to the cyclotron active

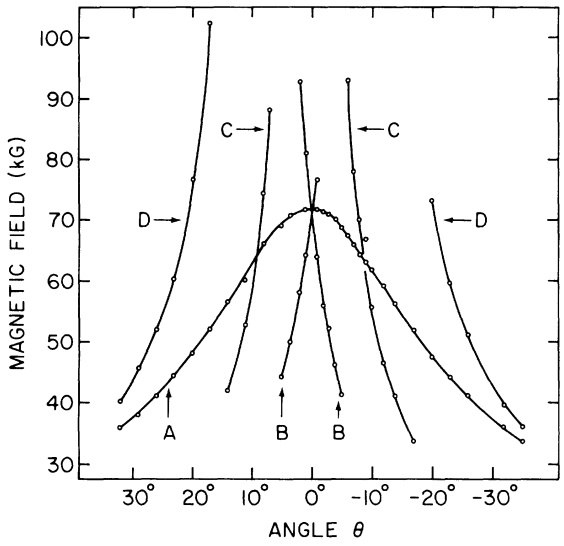

FIG. 9. Plot of the magnetic field positions vs magnetic field orientation corresponding to the absorption peaks observed at 890 GHz in Voigt configuration corresponding to Fig. 8. The zero has been chosen to correspond approximately with the bisectrix orientation. (A), Fundamental cyclotron resonance (C1 in Fig. 3). (B), Combined resonance (CO1 and CO2 in Fig. 3). (C), Spin-flip resonance (SF in Fig. 3). (D), Combined resonance (CO3 in Fig. 3). The solid line does not represent any theoretical fit.

polarization for the electrons. In the spectrum corresponding to this orientation in Fig. 10, the hole fundamental cyclotron-resonance absorption peak $C1$ is seen to be shifted about 1% toward higher magnetic fields compared with the case with H along the bisectrix axis. Otherwise the structure of this peak is similar to that in the bisectrix case except for the sharp structure in the high magnetic field side of this peak which corresponds to the combined resonance.

The peak marked $P3$ in the spectra of Fig. 11 that corresponds to $\psi = 24°$ can be identified as the combined resonance for the heavy electrons corresponding to the transition $0^+ \rightarrow 1^-$. This conclusion follows from the results of Sakai *et al.*[25] in which an experimental spin-splitting factor of about 0.7 is reported for these electrons in this orientation. Using the orbital masses and energy gaps of Table III we find that, for $H = 83$ kG (upper spectrum in Fig. 18), $\mathcal{E}_{1^-} - \mathcal{E}_{0^+} = 4.5$ MeV which is closed to the photon energy (4 MeV). This identification is also supported by the striking increase in the intensity of this absorption peak in going from 964 to 890 GHz. At around 75 kG the level 0^+ passes through the Fermi level so that the population of this level must be changing rapidly between these two cases. Thus the 0^+ level lies in the tail of the Fermi function for this transition in the 964-GHz spectrum.

C. Experimental investigation of the origin of the forbidden transitions

It is known from FIR magneto-optical studies in semiconductors[27] that multiple internal reflection in the sample can cause pseudostructure to appear around an absorption line as well as to produce absorption in the inactive mode. It is also known that impurities can produce structure, through impurity shifted cyclotron resonance,[28] for example. Dislocations, like impurities, can also produce new localized quasibound states[29] that could cause similar effects as impurities in the FIR magneto-optical spectra. Therefore, it was necessary to perform a series of experiments in order to determine as conclusively as possible whether or not these absorption peaks and their structure were due to intrinsic effects of pure

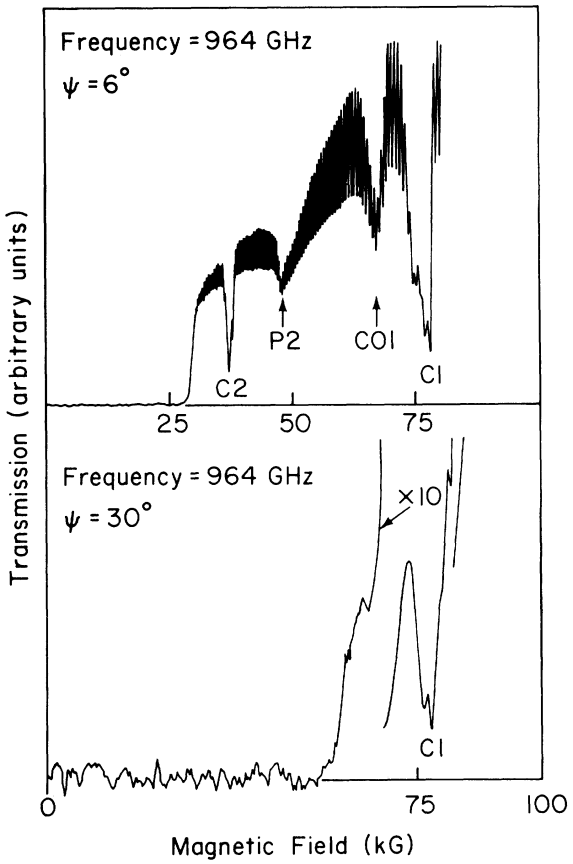

FIG. 10. Faraday configuration magnetotransmission spectra for two different magnetic field orientations on the trigonal plnae. Ψ is the angle between the magnetic field projection on the trigonal plane and the bisectrix axis. $\Psi = 30°$ corresponds to $\vec{H}$ parallel to the binary axis.

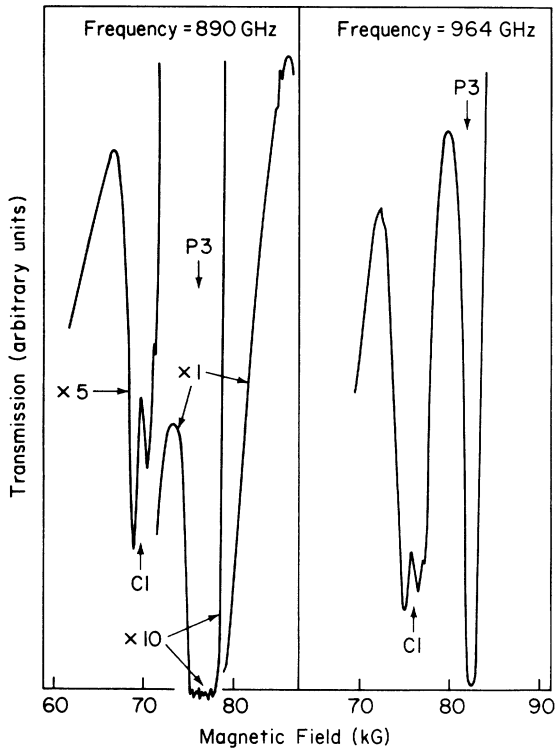

FIG. 11. Faraday configurations magnetotransmission spectra at two different frequencies. The magnetic field orientation corresponds to $\theta \sim 0°$ and $\Psi = 24°$. The sample thickness is 3.44 mm.

bismuth. With this aim in sight we studied (i) a wedged sample to sort out the effects due to the interference of the internally multireflected radiation, an effect that changes with the sample geometry, (ii) samples with different amounts of impurities, and (iii) plastically deformed samples to increase the density of dislocations and/or twinned layers.

For a wedged sample with an angle of 3° between faces no change was observed either in the presence of the absorption peaks or in their fine structure. However the Fabry-Perot interference oscillations were absent. Some broad structure in the spectra was attributable to the fact that for a 3° wedged sample the radiation emerging from the far side of the sample was refracted at a large angle from the light-pipe axis (the index of refraction of bismuth is 10–15) causing many reflections in the wall of the light pipe connecting the sample holder with the detector. Since the index of refraction of the magnetoplasma wave changes with the magnetic field, the exit angle also changes. This presumably caused broad pseudostructure to appear in the spectrum owing to differences in the attenuation and/or coupling of the radiation to the detector by the concentrating cone at different magnetic field strengths.

To test for impurity effects at 10-cm-long bisectrix plane single crystal was grown at a rather low speed (approximately 2 mm/h) in order to have a segregation coefficient as different from one as practically possible for the different impurities present in the as received 6–9 grade bismuth. Impurities with a segregation factor greater than one should concentrate in the seed end of the crystal, while impurities whose segregation factors are less than one concentration in the opposite end. Samples were cut from each end of the boule which were therefore expected to have different impurity contents. In these samples some changes in the over-all transmissivity were observed, but there were no changes in the appearance of

TABLE III. Bi parameters used in the calculations on magnetoplasma behavior.

Two-band-model energy parameters for electrons and holes[a]	
$E_F = 26.5$ meV[b]	$E_0 = 37.5$ meV[d]
$E_g = 13.6$ meV[c]	$E_0^h = 180$ meV[d]
Orbital effective-mass tensors at the Fermi level	
Electrons[e]	Holes[f]
$m_1 = 0.00705$	$M_1 = M_2 = 0.063$
$m_2 = 1.547$	$M_3 = 0.654$
$m_3 = 0.0295$	
$m_4 = 0.175$	
Electron-spin effective-mass tensor at the Fermi level[g]	
$m_1^s = .00488$	$m_3^s = .0525$
$m_2^s = 10.22$	$m_4^s = .628$
Hole effective g-tensor and spin-splitting factor at Fermi level[b]	
$g_{XX} = g_{YY} = 0$	$g_{22} = 63.2$
$\gamma = \frac{1}{2} g_{ZZ} m_c \lvert \sin\theta \rvert$	
Lattice dielectric tensor[i]	
$\epsilon_{XX} = \epsilon_{YY} = 100$	$\epsilon_{ZZ} = 60$

[a]See Fig. 2 for definition of these parameters.
[b]Determined by the condition $n_a^e + n_b^e + n_c^e + n^h$.
[c]From Ref. 44.
[d]Adjusted to give fair agreement with experimental results of Smith, Baraff, and Rowell (Ref. 23) on Shubnikov-de Haas oscillations from holes for H parallel to the bisectrix axis.
[e]From cyclotron resonance experiments (Ref. 43).
[f]From Ref. 45.
[g]From Smith, Baraff, and Rowell (Ref. 23).
[h]From our experiments.
[i]From Ref. 33.

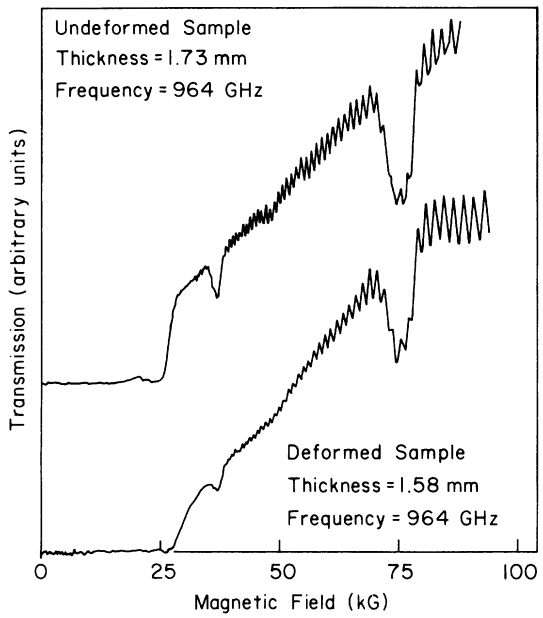

FIG. 12. Faraday configuration magnetotransmission spectra of Sample A. Before and after plastic deformation by compressing the sample along the bisectrix axis.

the peaks and their fine structure. Samples prepared from zone-refined bismuth processed as described in Sec. III were found to give a larger transmission, but again no change in the intensity of the absorption peaks or in their fine structure was found.

To test for the effects of mechanical deformation on the magnetotransmission spectra we prepared two differently deformed bisectrix plane samples. Sample A was prepared by squeezing it at room temperature along the bisectrix direction until a 10% permanent deformation was obtained. After etching, both twinned layers and slip planes were observed with an optical microscope. Sample B was bent by pushing it against a curved surface with a radius of curvature of 15 cm. The bending axis was parallel to the trigonal axis and the resulting plastic deformation corresponded to a 20-cm radius of curvature. This sample revealed a large number of twinned layers. It is difficult to determine what modes of deformation are operative in these samples and we were not attempting to study any specific kinds of defect structures. The interest in the study of these samples is that their magnetotransmission spectra give examples of the effects when large numbers of different defect structures are present.

Figures 12 and 13 show the magneto-optical transmission spectra in Faraday configuration for sample A and B, respectively. In each case the spectra obtained before and after plastic deformation are shown. A quantitative value for the change in transmission cannot be given since the experimental measurements were performed without a measure of the output of the laser for each run. But since the laser operating conditions were the same and the setting of detector sensitivity was also the same for both spectra shown in Fig. 12, we can say that the transmission for sample A, before and after deformation, was approximately the same at high magnetic fields. It can also be noted that the total strength of peak $C1$ has decreased by approximately 20% (about half of this can be accounted for by the decrease in thickness) and that its width and shape seems to have remained the same while peak $C2$ seems to have broadened after the plastic deformation. The largest change introduced by deformation is associated with the transmission edge, that starts at around 25 kG, which has become less sharp and a second not well-defined edge at around 59 kG seems to have appeared.

The spectrum for sample B after plastic deformation was taken with a sensitivity 10 times larger than for the spectrum of the undeformed sample. Therefore, transmission has decreased significantly. The position of the peak $C1$ has not changed, and it appears that the edge of transmission has moved to higher magnetic field (at approximately 60 kG).

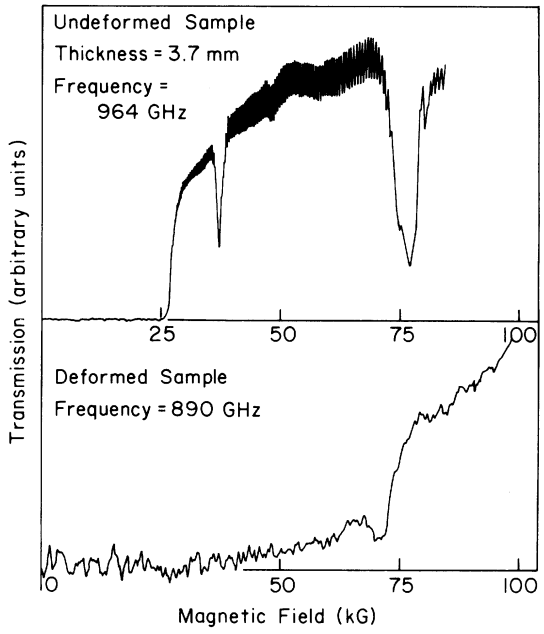

FIG. 13. Faraday configuration magnetotransmission spectra of Sample B. Before and after plastic deformation by bending the sample about the trigonal axis.

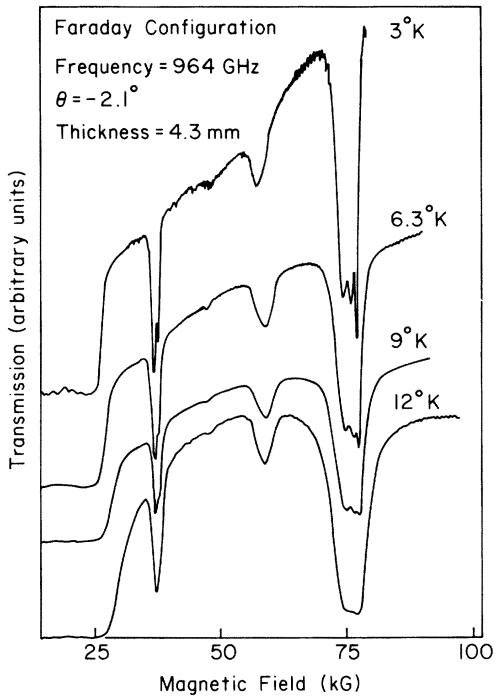

FIG. 14. Temperature dependence of the Faraday configuration magnetotransmission spectra.

D. Temperature dependence of the magneto-optical spectra

The temperature dependence of the transmission spectra of a bisectrix sample was studied in the Faraday configuration between 1.8 and 25 °K. Some of these results are shown in Fig. 14 where it is noticed that the fine structure of peaks $C1$ and $C2$ become less sharp and conspicuous at higher temperatures and essentially disappear at about 8 °K. As the temperature increases, the integrated absorption of the fundamental of cyclotron resonance increases somewhat, while the same effect is not so clearly observed for the second harmonic. There is no shift of the positions of the absorption peaks with temperature except for the combined resonance in the 3 °K case. However, this trace was made on a different sample than the others and the shift of the CO1 resonance is probably an orientation effect.

V. ANALYSIS OF THE EXPERIMENTS

A. Magnetoplasma waves

The transmission of far-infrared power observed in the experiments reported here is understood in terms of the excitation of propagating magnetoplasma waves in bismuth. The absorption lines identified and discussed in Sec. III C represent attenuation of these magnetoplasma waves due to weak electric-dipole–induced resonant transitions of the holes. The strength and line shape of the different absorption lines depend on the wave vector and electric field components of the propagating modes as is apparent from the matrix elements given in Appendix A. Therefore, in order to interpret the results fully it is necessary to know the characteristics of the propagating modes which we review in this section.

There have been extensive studies of magnetoplasma waves in bismuth at microwave frequencies in the 100-kG range.[30,31] At far-infrared frequencies the $\vec{q} \parallel \vec{H}$ (Faraday configuration) case has recently been investigated by Blewitt and Sievers.[4] Because there is an extensive literature on magnetoplasma waves in solid-state plasmas we need only to point out some features of the modes observed in our experiments that will be required for a discussion of our experimental results.

1. $\vec{q} \parallel \vec{H}$

In compensated plasmalike bismuth it is well known[32] that there are propagating magnetoplasma waves which are called Alfvén waves in the low-frequency limit. There are two polarization modes; the electron active mode which propagates for frequencies up to the first electron cyclotron resonance and the hole active mode which propagates up to the first hole cyclotron resonance.

To analyze the characteristics of these modes we have made several simplifying assumptions. We have used the local conductivity tensor derived for carriers with a parabolic dispersion relation. For the highly nonparabolic electrons the effective mass at the Fermi level is used. This gives an "average mass" which for $\hbar\omega \ll E_F$ should be sufficient to give an approximate description of the propagating magnetoplasma modes not too close to the electron cyclotron resonances. The Fermi level and carrier densities at each magnetic field have been calculated self-consistently as described elsewhere,[23] and we have used the approach of Takano and Kawamura[31] to account for the shift of the lowest electron Landau level with magnetic field.

For the magnetic field in the binary plane of bismuth, the case of interest in this work, two of the three electron pockets are equivalent so that we have a magnetoplasma with two electron cyclotron frequencies, ω_{ce}^1 and ω_{ce}^2, and one hole cyclotron frequency ω_{ch}. Also for orientations such that θ (Fig. 2) satisfies $|\theta| < 35°$, $\omega_{ch} \ll \omega_{ce}^1$, ω_{ce}^2, which is the case for our experiments.

In Fig. 12 an example of the results of a calculation of several important properties of these modes with the above described approximations is shown. The parameters used in the calculations are those in Table III. The propagating mode in our magnetic field range is the electron active mode since the hole active mode is strongly at-

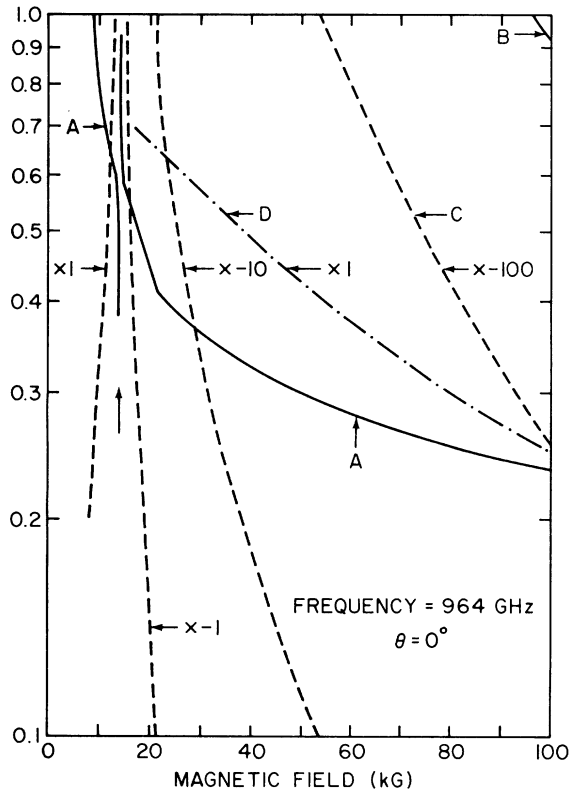

FIG. 15. Characteristics of the propagating mode in the Faraday configuration calculated in the local limit. (A) $q\times10^{-4}$ cm^{-1} vs H for the electron active mode polarization. The arrow indicates the position at which the magnetoplasma resonance occurs. (B) $q\times10^{-4}$ cm^{-1} vs H for the hole active mode polarization. (C) Real part of E_z/E_y for mode (A). (D) Imaginary part of E_x/E_y for mode (A).

tenuated. It is seen in Fig. 15 that no absorption takes place at the hole cyclotron-resonance frequency in the electron active mode. However, some absorption has been observed in this mode in microwave-frequency experiments which has been explained in terms of a mode-mixing effects produced by the combination of the nonlocal effects in the conductivity tensor and the anisotropy of the hole Fermi surface. For the hole cyclotron-resonance harmonics and spin-flip and combined resonances no absorption is predicted from these effects.

Therefore, except for the fundamental hole cyclotron resonance, it should be sufficient to use the local approximation to characterize the electron active mode since $qR_c \ll 1$ (R_c is the cyclotron radius). This is the approximation that we will adopt in this paper for the calculation of the line shapes of the weak transitions observed in our experiments.

2. $\vec{q}\perp\vec{H}$

In the Voigt geometry the propagating magnetoplasma waves in bismuth have not been studied at far-infrared frequencies. However, extensive microwave studies have been reported.[33] With the same approximations described above in the conductivity tensor only one propagating mode is predicted which is called the "fast" magnetosonic wave. This mode propagates for frequencies up to the lowest hybrid frequency ω_{hy} ($\omega_{hy}\approx(\omega_{ch}\omega_{ce}^1)^{1/2}$ for H in the binary plane).[34] For isotropic carrier masses the fast magnetosonic mode is polarized transverse to the magnetic field. However, for an anisotropic system such as bismuth the mode is never really transverse and only approximately so in special cases (H parallel to bisectric axis, for example).

When the nonlocal character of the conductivity tensor is considered in the Voigt geometry, additional modes appear that propagate close to the cyclotron-resonance frequencies which have been called cyclotron waves.[32] For an isotropic system these waves can be polarized transverse to the magnetic field (extraordinary waves) and along the magnetic field (ordinary waves). Akahane and Uemura[35] have discussed magnetoplasma waves for a multicomponent anisotropic plasma like bismuth. Experimental studies of bismuth at microwave frequencies have been reported by Nakahara *et al.*[36] and by Naberezhnikh *et al.*[37] These studies show that the magnetosonic wave interacts with the cyclotron waves close to cyclotron-resonance harmonics producing hybridized modes. The case of q parallel to bisectrix axis, corresponding to our experiments, has been studied at microwave frequencies by Nakahara.[36] The hybridization effect was found to be very strong at the second harmonic of hole cyclotron resonance but almost negligible near the fundamental. Because of this hybridization total reflection can occur in a small interval of ω/ω_{ch} near the second harmonic, which accounts for the large attenuation near the second harmonics observed in our far-infrared experiments (Fig. 8). Away from the hole cyclotron-resonance harmonics the hybridization effects will be small, and local calculations like these described for the Faraday geometry are adequate to obtain the characteristics of the propagating magnetosomic wave for our line shape calculations.

B. Experimental determination of the effective Hamiltonian

To find the best parameters for $\mathcal{H}_{eff}$ it is possible, in principle, to use the resonance positions, the linewidths, and the oscillator strengths for all the observed lines. However there are limitations to the accuracy of the theory which make such a

program unjustified at this stage. First, the effective Hamiltonian has too many parameters to reasonably attempt a unique fitting to the experiments. In addition, there are uncertainties in the marking of the proper resonance position owing to the electron-electron interaction effects on the line shapes and inaccuracies in the transitions matrix elements owing to the perturbation expansions of wave functions [Eq. (11)]. The electron-electron interaction effects will be discussed in II.

Because of these limitations we have chosen to fit only the positions of the resonances by adjusting the $\mathcal{K}_{\text{eff}}$ parameters self-consistently within the framework of theoretical calculations of these parameters. The line shapes and intensities are then calculated from $\mathcal{K}_{\text{eff}}$ and compared with the experiments. Also, the cyclotron masses and g factors corresponding to microwave and Shubnikov-de Haas measurements are deduced and compared with experiments.

1. Line shape calculations

Calculations of the line shapes have been done excluding electron-electron interaction effects and using the approach described in Sec. II. In order to compare the experimental results with the calculations, we have marked the position of the peaks at the magnetic field that corresponds to the maximum absorption, since we believe this best represents the combined effect of the dependence on momentum and the Landau quantum number of the joint density of states and transition matrix elements when the e-e interaction is neglected. In II it will be seen that the shape of absorption lines is strongly modified by the e-e interaction. Consequently the comparison between the experimental position of the absorption peak and the calculated one without e-e interaction effects determined at the point of maximum absorption is not strictly justifiable. Nevertheless since the e-e interaction effects amount to a shift of the strongest absorption point by (2–3)% (not including self-energy corrections) this comparison is at least good enough to determine a first approximation of the values of the parameters of $\mathcal{K}_{\text{eff}}$. The inclusion of self-energy corrections owing to e-e interaction produces a shift in the position of the absorption peaks that can reach values as high as 10%. However, the effective Hamiltonian can be regarded as already including this effect in the lattice potential in an average way.

In the calculations of the line shape it is only feasible to take the magnetic field as fixed and to calculate the absorption as a function of frequency. The experimentally observed values of the magnetic field corresponding to the maximum of the absorption peak under consideration have been taken. On the other hand, the experiments were performed at fixed frequency and sweeping the magnetic field. Since it would be too difficult and costly to perform the calculations in this way, we have instead made a semiempirical conversion between the frequency scale in the calculations and the magnetic field scale in the experiments. The scaling law for the conversion of frequencies into magnetic fields is

$$H = H_0 \omega_0 / \omega \ , \tag{16}$$

where H_0 and ω_0 are the magnetic field and the frequency that correspond to the absorption peaks, and ω is the calculated frequency for a given transition corresponding to the magnetic field H_0. Then H is the magnetic field at which the transition, which occurs at the frequency ω when the magnetic field is kept fixed to the value H_0, is observed if radiation of frequency ω_0 is used.

This conversion of frequencies into magnetic fields is only strictly correct for a peak width that is vanishingly small in comparison with its position. It omits correction terms to the dispersion relation during the small shift in magnetic field. Also, the change in the relative positions of the Landau level ladders and the Fermi level is ignored. This effect can cause rapid changes in the line shapes if the highest occupied Landau level passes through the Fermi level while the field is swept through the resonance. These effects are small for most of our lines which are only 2–3% in width. Moreover, these effects are more important in modifying the line shapes than in affecting their widths, and so we are justified in ignoring them in these calculations which do not include the electron-electron interaction effects. In Fig. 16 we show, as examples, the calculated line shape for the case of the 2nd harmonic of cyclotron resonance in the Faraday geometry for $\theta = -1.50$ at 171 μm and the spin-flip resonance in the Faraday geometry for $\theta = -8°$ at 311 μm. The experimental results are shown in Figs. 5 and 6. In the case of the 171-μm spectrum the fine structure from electron-electron interaction effects is absent. From the calculated line shapes we have also calculated the corresponding integrated absorption defined as

$$\Lambda \equiv \frac{H_0}{\omega_0} \int_0^\infty d\omega \, \alpha(\omega) \cong \int_0^\infty dH \, \alpha(H) \ . \tag{17}$$

2. $\mathcal{K}_{\text{eff}}$ parameters

In Golin's study[5] of the bismuth band structure by the pseudopotential method he notes that the matrix elements of the velocity operator $\vec{\Pi}$ at the T point of the Brillouin zone are less sensitive to small changes in the pseudopotential parameters than are the energy gaps. This observation provides the justification for his procedure of deter-

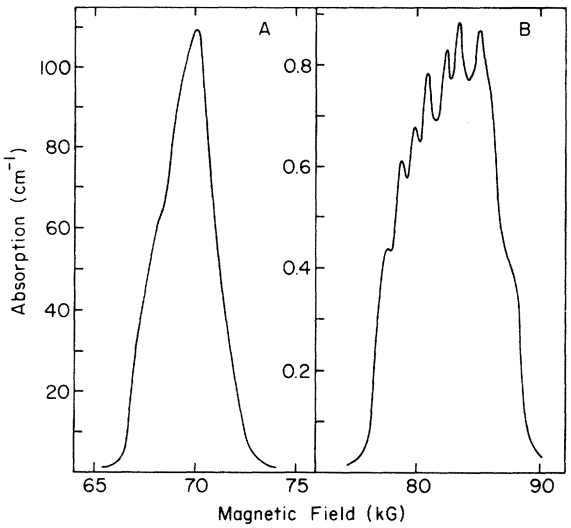

FIG. 16. (A) Calculated line shape for the second harmonic of cyclotron resonance in Faraday configuration at 1746 GHz, $\theta = -1.5°$, $\tau = 50 \times 10^{-12}$ sec, $9 = 4710$ cm^{-1}. (B) Calculated line shape for the spin-flip resonance in Faraday configuration. The experimental spectrum is at 964 GHz, $\theta = -8°$, $\tau = 50 \times 10^{-12}$ sec, $9 = 2500$ cm^{-1}. The experimental trace is shown in Fig. 5.

mining the energy gaps by fitting the experimental effective masses and spin-splitting factor using the $\vec{\Pi}$ matrix elements obtained from his calculation. From the one-band effective Hamiltonian to second order in $\vec{P}$ (the effective-mass approximation) it is possible to determine Δ_1, Δ_2, and Δ_4 (Fig. 1). Golin's results for these parameters are shown in Col. 2 of Fig. 1. Using a six-band $\vec{k} \cdot \vec{P}$ perturbation theory Hamiltonian, Bate *et al.*[1] obtained an expression for the hole dispersion relation for $H = 0$ in which the gaps Δ_3 and Δ_5 were also involved. Fitting their Shubnikov–de Haas results on tin-doped bismuth they obtained the band parameters in Col. 2 of Fig. 1.

We first redetermined the parameters Δ_1, Δ_2, and Δ_4 following Golin's method using the more recent values of the hole effective masses and g^2 tensor shown in Table III. With these energy gaps the coefficients A, B, C, D, G_1, G_2, and the $G_{\alpha\beta,ij}$ were calculated from the $\vec{P} \cdot \vec{\Pi}$ perturbation expression with the help of a computer. With the resulting parameters the full $\mathcal{H}_{eff}$ [Eq. (3a)] then predicts different effective cyclotron mass and spin-splitting factors, and moreover the positions of the observed resonances in the far-infrared are not correctly predicted. It is therefore necessary to readjust the parameters to see if the Hamiltonian can properly describe the experiments. Since there are 27 parameters involved it is not practical to vary each of them independently. Also none of the parameters are sufficiently unimportant that we can eliminate them from the Hamiltonian to simplify the problem. We therefore chose to reduce the number of parameters by introducing four scaling factors; υ_1 for α_1 and α_2; υ_2 for G_1 and G_2; υ_3 for A, B, C, and D; and υ_4 for the $G_{\alpha\beta,ij}$. This assumes that Golin's calculation, which already gives a good approximation to these parameters, does give the correct relationships between the parameters in each of the four sets.

The positions of the spin-flip resonances at different orientations were first fit by adjusting υ_2 and υ_4. Then υ_1 and υ_3 were adjusted to fit the cyclotron-resonance harmonics. From the resulting new values of the effective masses and spin splitting factors entering the second-order Hamiltonian $\mathcal{H}_1$, the "experimental energy gaps" were recalculated following Golin's procedure. The results for Δ_1, Δ_2, and Δ_4 are shown in the last column of Fig. 1. Δ_3 and Δ_5 were estimated by scaling the values calculated by Golin in proportion to the ratio of the values of Δ_1, Δ_2, and Δ_4 in Cols. 1 and 3 of Fig. 1.

With these energy gaps we recalculated the coefficients of A, B, C, D, and $G_{\alpha\beta,ij}$. These calculated values are shown in Table I. With these new coefficients we readjusted the values of υ_1, υ_2, υ_3, and υ_4. The final values of the parameters of the effective Hamiltonian obtained in this way are shown in the last column of Table I.

From Table I it is seen that the $\mathcal{H}_2$ parameters calculated from Golin's matrix elements for $\vec{\Pi}$ and the energy gaps of Fig. 7 are approximately twice as large as the values of the parameters that fit the experiments. It would be possible to reduce the calculated values of the coefficients of the fourth-order terms by a factor of 2, without affecting $\mathcal{H}_1$, if we scale up the value of each matrix element calculated by Golin by a factor of $\sqrt{2}$ and scale up each energy gap by a factor of 2. These questions must await experimental determination of the gaps.

It is also interesting to note that Bate *et al.*[13] obtained a good fitting for the Sh-dH experiments in Sn-doped Bi with a $\vec{k} \cdot \vec{p}$ perturbation theory calculation using Golin's matrix elements and the energy gaps shown in Column 2 of Fig. 1. We note here a disagreement with our results for the parameters for $\mathcal{H}_2$. This disagreement is similar to that found between the results for the energy gap extracted from Shubnikov-de Haas experiments in tin-doped bismuth when they are interpreted in terms of the two-band model ($E_g = 66$ MeV) and the energy gap obtained by interpreting the position of the cyclotron resonances in our experiments ($E_g \cong 200$ MeV). This disagreement suggests that the electronic structure of the hole pocket is chang-

TABLE IV. Experimental and calculated absorption peak positions, widths, and integrated intensities; Faraday configuration only.[a]

θ	Transition	Freq. (GHz)	H_{expt} (kG)	H_{calc} (kG)	ΔH_{expt} (kG)	ΔH_{calc} (kG)	Λ_{expt} (cm^{-1} kG)	Λ_{calc} (cm^{-1} kG)	Obs.[b]
−21.5°	SF	964	28.9 (29.8*)	29.0	1.4	1.3	0.90	0.36	
−21.5°	C1	964	49.9	51.0	6.1	5.1	...	...	
−21.5°	CO3	964	71.8	71.4	...	...	0.89	0.73	
−13.0°	SF	964	48.5 (50.0*)	48.8	4.3	4.7	5.5	1.9	
−13.0°	C1	964	63.1	63.1	7.4	...	...	...	
−8.0°	SF	964	81.9 (84.0*)	83.7	10.0	13.6	19.0	8.21	
−8.0°	C1	964	71.0	71.0	6.7	6.0	14.8	12.8 7.8	η=0.350 η=0.355
−8.0°	C2	964	35.0	33.3	1.9	...	6.45	83.1	
−3.4°	C1	1612	(130) 134*	134.5	15.0	14.0	...	...	
−3.4°	C2	1612	62.2	62.9	5.8	5.3	...	...	
−3.4°	C3	1612	41.0	41.0	2.9	3.0	...	...	
−2.3°	C1	452.2	(34.6) 34.9*	34.0	3.3	3.0	...	...	
−2.3°	C1	525.5	40.6 (41.3*)	39.7	3.6	3.1	...	...	
−2.3°	CO1	525.5	32.45	30.44	1.9	2.5	...	0.104	
−2.3°	CO2	525.5	57.5	56.8	1.3	3.6	...	0.902	
−2.3°	SF	337.0	(85) (104) (111) 121	94.3 99.5 105.7 112.3	... ...	... ...	14.0	10.0	
−2.1°	C1	890	(69.6) 71.6*	69.1	7.0	5.0	...	...	
−2.1°	C2	890	34.0 (34.8*)	33.3	2.3	2.4	...	...	
−2.1°	C1	964	(74.9) 77.5	76.0	6.7	6.0	14.8	6.51	η=0.328
−2.1°	C2	964	36.8 (37.6*)	36.1	3.1	2.5	4.8	83.1	
−2.1°	CO1	964	60.3	57.1	7.0	3.9	2.9	2.02	
−1.5°	C2	1746	69.5	69.8	5.7	6.0	10.5	380	
−1.5°	C3	1746	46.0	45.1	3.8	3.4	...	...	
21.0°	C1	964	50.5	50.2	6.0	...	...	...	
21.0°	CO3	964	(73.4*) (74.4*) 77.4	74.8	...	...	>25	4.2	

[a]The calculated values have been obtained using the Hamiltonian (3a)−(3c) with the set of parameters shown in the last column of Table I.

[b]$\eta = |E_x/E_y|$.

ing as Sn is added to bismuth.

In Table IV we present the value of the experimental and calculated resonance positions in the Faraday configuration using the parameters of Table I.[38] When the observed absorption peak shows fine structure we also include the position of the other maximum, written between brackets, noting the sharpest structure with a star (*). The

calculated values for the integrated intensity Λ and some experimental values are also shown in Table IV. The agreement between the calculated and the observed positions with the parameters of the last column of Table I is reasonably good. Also, the calculated and observed integrated absorption for the spin-flip and combined resonance absorption peaks agree in order of magnitude which is also a satisfactory agreement considering the approximations and the assumptions that have been made in the theory. It is interesting to note that the calculation does show the remarkably asymmetric behavior of the intensity the absorption peak CO3 with ϑ. (See Figs. 5 and 8.) In the case of the 2nd and 3rd harmonics of the cyclotron resonance, the calculated integrated absorption is about an order of magnitude larger than the observed one.

The case of the second harmonic of cyclotron resonance is interesting because in this case, for the orientation that corresponds to $\theta = 0$, the value of the calculated absorption depends only on the parameter B of the effective Hamiltonian $\mathcal{H}_2$. The calculated absorption could be made to agree with the observed one by reducing this parameter by about a factor of 4. However, we think that the validity of our theoretical calculations (using first-order perturbation theory) for the transition matrix elements is rather limited, so that we prefer not to give a strong weight to estimations of the value of the parameters of $\mathcal{H}_1$ through comparisons of experimental and calculated absorption strengths at this stage. Similarly the calculated absorption for the third harmonic of the cyclotron resonance depends on several parameters (A, C, and D) of the Hamiltonian $\mathcal{H}_1$ and is very sensitive to their relative values.

The calculated absorption for the fundamental of cyclotron resonance is not very reliable since the result is very sensitive to the ratio of the x and y components of the electric field of the propagating mode which determines the amount of the cyclotron-active mode present. We present the result for a value of E_x/E_y chosen to give the minimum absorption. This value of E_x/E_y differs by 6% from the value calculated as described in Sec. V A. If the calculated value for E_x/E_y is taken, the calculated absorption strength comes out to be two orders of magnitude larger than the one reported in Table III. This sensitivity to E_x/E_y is due to the fact that the expression for the transition matrix element, given by Eq. (A6), involves the difference $D = iE_x^*\sqrt{\alpha_1} - E_y^*\sqrt{\alpha_2}$ with a factor that is of zero order in the parameters of $\mathcal{H}_2$ (considered to be a perturbation) and first order in the parameters of $\mathcal{H}_1$ (the zero-order Hamiltonian). If holes in Bi could be described by $\mathcal{H}_1$ only, then it can be shown that $E_y^* = i(\alpha_1/\alpha_2)^{1/2}E_x^*$ at the position of resonance and then D would be zero. Since the magnetoplasma-mode calculation is done using a two-band model for holes it is expected to give only an approximate value for E_x/E_y. Because of these problems the fundamental of cyclotron resonance is not a very good case for line-shape analysis.

Table IV also shows the calculated and observed widths for the various kinds of observed transitions. The widths were measured close to the bottom of the absorption peak, which is not a rigorous procedure but it gives some account for the spread in the resonances due to nonparabolic effects. That the widths come out reasonably well from the Hamiltonian adjusted to fit only the positions of the absorption lines is regarded as confirming evidence that a reasonable approximation to $\mathcal{H}_{\text{eff}}$ has been found.

C. Cyclotron masses and spin-splitting factors

For the case of H parallel to the trigonal or bisectrix axis the expressions for the effective cyclotron masses in the limit of vanishing H (the case of microwave experiments) and for the extremal sections of the Fermi surface can be easily derived from Fq. (4) and Eqs. (6a) and (6b) using the relation

$$\frac{\hbar eH}{m_0 c}\,\frac{1}{m_c} = (\mathcal{E}_{n,k_z,s} + \delta\mathcal{E}^{\text{orb}}_{n,k_z})_{k_z} = 0 \\ - (\mathcal{E}_{n-1,k_z,s} + \delta\mathcal{E}^{\text{orb}}_{n-1,k_z})_{k_z} = 0 \qquad (18)$$

and considering $n \gg 1$ and $n\hbar\omega_c = \mathcal{E}_F$. The result for H parallel to the bisectrix axis is

$$m_c^{\text{bx}} = (M_1 M_2)^{1/2}[1 - 3m_0^2\mathcal{E}_F(AM_1^2 + DM_3^2 + 2CM_1M_3)]\,, \qquad (19)$$

and for H parallel to the trigonal axis,

$$m_c^{\text{tr}} = M_1(1 - 8m_0^2 M_1^2 \mathcal{E}_F A)\,. \qquad (20)$$

Table V shows the values for these masses taking the parameters of the second and third columns of Table I and $\mathcal{E}_F = 11$ MeV.

It can be seen that the parameters of the last

TABLE V. Comparison between the calculated cyclotron masses using the parameters of Table I and the experimental values determined by Édelman and Khaikin (EK) (Ref. 45).

m_t^{Tr}	0.0758[a]	0.0646[b]	0.063 ± .001[c]
m_c^{Bx}	0.2291[a]	0.2030[b]	0.203 ± .004[c]

[a]Result of the calculations using the H_{eff} parameters shown in column 2 of Table I.

[b]Result of the calculations using H_{eff} parameters shown in column 3 of Table I. Our experimental values.

[c]Experimental values determined by EK.

column of Table I also fit the values of the cyclotron masses determined in the low magnetic field experiments reasonably well. However, these results must be interpreted cautiously. The results for m_c^{bx} are likely more reliable than for m_c^{tr} because the parameters for $\mathcal{H}_{eff}$ were determined mainly from data close to the bisectrix axis. Also, the electron-electron interaction effects complicate the interpretation. The experimental masses should be the dressed masses while the masses from $\mathcal{H}_{eff}$ determined from the FIR experiments are probably closer to the bare mass.

Although the concept of a spin-splitting factor, $\gamma = \omega_s/\omega_c$ becomes imprecise for a nonparabolic Hamiltonian, it can still be useful for describing the average ratio of spin splittings to Landau level spacings if it gives with some accuracy the positions of the spin-flip and combined resonances. Also, the far-infrared results are then more easily compared with the microwave and equilibrium measurements of the g factors.

If is is assumed that the dispersion relation for holes is parabolic as given by Eq. (4), the separation between magnetic levels is constant in this model for all k_z and proportional to the magnetic field. Therefore a value for γ could be determined from the experiments using the following relations·

$$\gamma = H_{C1}/H_{CO1} - 1 , \tag{21a}$$

$$\gamma = 1 - H_{C1}/H_{CO2} , \tag{21b}$$

$$\gamma = H_{C1}/H_{CO3} + 1 , \tag{21c}$$

$$\gamma = H_{C1}/H_{SF} . \tag{21d}$$

In the Voigt configuration the width of the absorption peaks, in this model, would be entirely due to broadening of the Landau levels produced by scattering processes with phonons or impurities. However, the experimental results show a rather broad structure in the absorption peaks with a total width that cannot be entirely attributable to this effect since we observe very sharp features in them indicating that $\omega\tau \gtrsim 100$. The width of these absorption peaks must be due, then, to dispersion relation effects and electron-electron interaction effects. If we ignore electron-electron interaction effects, the experiments would then reflect a departure from the above simple model which we call "nonparabolicity effect".

The broadening of the absorption peaks by this nonparabolicity effect makes it difficult to define the position of an absorption peak in terms of a value for the magnetic field or frequency around which it occurs. Although only a better model than that defined by Eq. (4) can resolve the ambiguity of marking the position of the absorption peaks it is interesting to interpret the experimental results with this simple "parabolic" dispersion relation. We will mark the absorption peaks as described earlier (Sec. IV A). This marking is self-consistent in the sense that the values of γ obtained using expressions (21a) and (23b), when two kinds of combined resonances are observed on the same spectrum, differ by no more than 2%. A similar agreement is found when both combined resonance and spin-flip resonance are observed in the same spectrum.

The plot of γ as a function of the orientation of the magnetic field on the binary plane obtained in this way from our experiments is shown in Fig. 17. Close to $\theta = 0°$, the experiments indicate that $\gamma \cong 0$. If it is assumed that γ is exactly zero at $\theta = 0°$ then, since g^2 must be a tensor in this "parabolic" model, we get the following expression for γ:

$$\gamma = \tfrac{1}{2} g_{zz} m_{cY} (\rho + \cot^2\theta)^{-1/2} , \qquad g_{zz} = (G_1^2 + G_2^2)^{1/2} , \tag{22}$$

derived using Eqs. (5e) and (5g) and where m_{cY} is the cyclotron effective mass for H along the bisectrix axis and $\rho = M_3/M_1$.

Choosing m_{cY} and ρ to fit approximately our experimental results for the position of the fundamental cyclotron resonance as a function of the

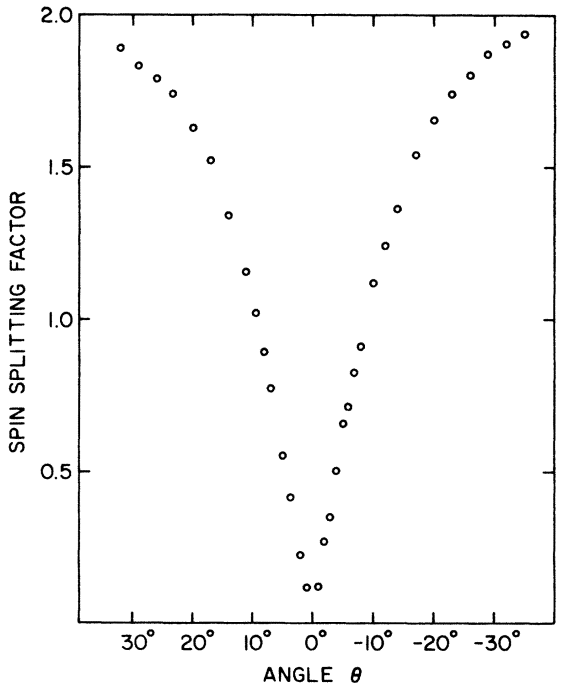

FIG. 17. Experimental hole spin-splitting factor determined by assuming a parabolic dispersion relation for holes as described in the text. The zero for the horizontal scale has been chosen to correspond approximately with the bisectrix axis.

magnetic field orientation on the binary plane shown in Fig. 8, we get $m_{cY} = 0.226$ and $\rho = 11.8$. Using these values and fitting approximately the values of γ plotted in Fig. 13, we get $g_{ZZ} = (63.2 \pm 1.8$.

The value of γ for H parallel to the trigonal axis ($\theta = 90°$) from Eq. (22) with the above parameters is 2.08 ± 0.06. We can also derive an expression for γ from

$$\gamma^{tr} = \frac{1}{2} \frac{g_{zz}}{\alpha_{zz}} [1 + A\mathcal{E}_F(3M_1^2 + 2M_1M_3 + 3M_3^2)]^{-1} . \tag{23}$$

Using the parameters of the last column of Table I we find $\gamma^{tr} \cong 2.3$. The values reported in the literature for this orientation are always less than two ($\gamma = 1.94$,[23] $\gamma = 1.86 \pm 0.02$,[25] $\gamma = 1.87 \pm 0.01$).[26] This disagreement is outside the range of experimental error and suggests the need for reexamination of the interpretation of the Sh–dH experiments.

D. Fine structure on the absorption lines

In the experiments the absorption lines generally appear to be composed of one or more sharp features ($\Delta H/H \sim 0.01$) as well as a broad absorption peak ($\Delta H/H \sim 0.1$). These sharp-fine structure features are not found in the line-shape calculations in the single particle approximation. In Sec. IV C we described a series of experiments aimed to resolve whether or not this fine structure is related to sample geometry, impurities or dislocations, or other crystal irregularities. The conclusion of these experiments was that there was no evidence that these effects were responsible for the observed structure.

There are two intrinsic effects that could be considered as candidates for the source of this fine structure that we want to discuss here. One is related with phonon-assisted transitions and the other with the electron-electron interaction.

The analysis of the process in which an acoustic phonon is absorbed or emitted in the transitions has been done by Weiler *et al.*[39] and we will draw on their results throughout this discussion. Let us assume that the hole dispersion relation is parabolic and neglect spin. Let us also assume that H is along the bisectrix axis and that the electron-phonon interaction is sufficiently small that perturbation theory is applicable. Since we are looking for absorption in the inactive-mode polarization the second-order process must be considered in which first, a virtual excitation of a hole from the initial state occurs with the simultaneous emission or absorption of a phonon, and then a photon with the cyclotron-resonance inactive polarization is absorbed and the hole falls to the next lower Landau level. From the analysis by Weiler *et al.* a peak in the absorption is expected when the component of the phonon momentum $\vec{Q}$ along the magnetic field is zero (the photon momentum is being neglected) since the joint density of states will have a sharp maximum for this case. The absorption is zero for $Q_\perp = 0$ and there can be maxima for certain values of $Q_\perp$. Therefore if the unshifted cyclotron resonance is seen, we expect to find satellites at either side related with these acoustical phonon-assisted processes and their relative intensities should be temperature dependent.

Examining the line shapes of the absorption lines obtained in our experiments, the best candidate to support this picture is the triplet structure of the $C1$ absorption line which is seen in Faraday configuration for $\theta = -2.1°$ (Fig. 5). Here we could identify the central peak as the unshifted cyclotron resonance produced by the mode-mixing mechanism, for example, and the other two peaks as due to the acoustical phonon-assisted resonance. However, the line shape of this peak does not look like a triplet in the Voigt configuration (Fig. 8). Other cases are even harder to understand in terms of the acoustic-phonon process; for example, the sharp feature on the high-field side of the spin-flip transition in the Faraday configuration (Fig. 5) and the absence of this feature in the Voigt configuration (Fig. 8).

We have not done any detailed line-shape analysis or temperature-dependence studies for the acoustic phonon-assisted resonances to conclusively eliminate it as an explanation for the observed fine structure. However, the detailed success of the electron-electron interaction picture presented in the subsequent paper is an indication that the acoustical phonon-assisted resonance is not responsible for the fine structure observed in our experiments.

In the electron-electron interaction picture the final state interactions of the electron-hole pairs produced in the optical absorption produces collective states with a different excitation spectrum than that given by the noninteracting particle picture. For the direct band-gap absorption in semiconductors this process leads to excitonic states and corresponding excitonic structure on the absorption edges. We are considering similar excitonic effects associated with the transitions between the magnetic subbands in bismuth. This case has been treated semiclassically and semiphenomenologically for isotropic metals within the Landau-Silin theory of Fermi liquids. This theory also predicts collective states with energies different than the single-particle states and these effects have been seen in microwave experiments on the alkali metals. The new features involved in our experiments are the anisotropic carrier

masses and their highly quantized condition ($\hbar\omega \sim E_F$ and $\hbar\omega_c \sim E_F$). Since Fermi-liquid theory assumes $\hbar\omega \ll E_F$ and $\hbar\omega_c \ll E_F$ it is inappropriate for these measurements.

We have developed a microscopic theory of these excitonic effects within the generalized random phase approximation. A preliminary account of this interpretation has been published elsewhere.[6] We will present a more thorough analysis of these effects in a separate paper.[7]

VI. CONCLUDING REMARKS

We have found that a satisfactory description of the hole pocket dispersion laws is provided by the one-band effective Hamiltonian adjusted to fit the far-infrared resonance studies. For the purposes of this first attempt the accuracy of the one-band Hamiltonian and the first-order perturbation theory calculation of its eigenvalues is adequate for obtaining reasonable quantitative agreement with the far-infrared experiments and the low-frequency cyclotron masses and spin-splitting factors for the holes. No doubt these results could be improved somewhat by extending the far-infrared experiments to a larger range of orientations and frequencies. Indeed it is noteworthy that only the 311-μm Faraday geometry data which were taken between $-22° < \theta < 22°$ were used to fit the parameters of the effective Hamiltonian in this work. At higher frequencies, which would have permitted a larger range for θ, measurements were not successful because the greater attenuation of the magnetoplasma waves for this case made the transmitted signal too small for spectroscopy in the Voigt geometry. However, any attempt to improve the characterization of the hole pocket dispersion laws should incorporate the more exact six-band effective Hamiltonian and its exact eigenvalues. It is possible that an exhaustive far-infrared study would enable direct experimental determination of the many parameters entering the effective Hamiltonian without recourse to the scaling scheme based on Golin's interband matrix elements that we have used. However, the problem that remains with any such program would be to properly incorporate the many-body effects on the calculated absorption line shapes. Otherwise as we will see in II the (2–10)% uncertainty in the proper "resonance field" position would remain.

As we have seen, the effective Hamiltonian does not account for the very striking fine structure that is observed on many of the absorption lines. It is always possible to artificially construct a dispersion relation that will fit a particular resonance line shape. However, these model dispersion relations are then totally inadequate for describing the other resonance lines in our wealth of spectral data. We interpreted these fine-structure features in terms of electron-electron interaction effects in an earlier preliminary report on this work. In this picture these features are excitonic effects which arise from the final state interactions of the electron-hole pairs produced in the optical absorption process. A more detailed analysis of these effects will be presented in a subsequent paper[7] (II). Indeed a proper description of these excitonic effects required a knowledge of the carrier dispersion relations and transition matrix elements calculated in this paper. The electron-electron interaction effects are found to account for the diverse fine-structure features in the far-infrared experiments in a natural and simple way.

Complications arising from the highly anisotropic band structure of bismuth and difficulties in testing the electron-electron interaction effects correctly under conditions of high magnetic fields make an exact calculation of the absorption line shape and position impossible at this stage. We must therefore be satisfied for the present with the rather empirical peak-marking procedure employed in this paper and the resulting approximate determination of the carrier dispersion laws.

The results of this paper should therefore be regarded as indicative of the kinds of corrections to the carrier dispersion laws produced by the higher-order terms in the $\vec{P}\cdot\vec{\pi}$ perturbation theory and giving the approximate magnitude of these nonparabolic corrections for the hole pocket in bismuth. These effects are seen to be non-negligible. The approach we have used should be easily adapted to other semimetals and narrow-gap semiconductors. Particularly, these experiments should be useful for BiSb alloys, PbTe, SnTe, PbSe, and SnSe and the alloys of these Pb and Sn salts.

ACKNOWLEDGMENTS

The authors are grateful to Dr. R. J. Wagner and the Naval Research Laboratory for the use of their high magnetic field and optically pumped far-infrared laser facilities for some of our measurements. We also thank Dr. U. Strom and Steve McKnight for their assistance in making these measurements. We are also grateful to the Center of Materials Research of the University of Maryland for providing the initial support for this research and for the use of their Magnet Central Facility. Finally, we would like to acknowledge the numerous helpful and stimulating discussions with Dr. R. E. Prange, Dr. V. Korenman, and Dr. A. J. Sievers and his research group.

APPENDIX: MATRIX ELEMENTS FOR CYCLOTRON RESONANCE, SPIN-FLIP RESONANCE, AND SEVERAL KINDS OF COMBINED RESONANCES

A. Fundamental cyclotron resonance

The matrix elements are calculated as outlined in Sec. II C.

$$\mathcal{H}_1' = \frac{1}{2}\frac{e}{i\omega}\left[\left(\frac{\hbar\omega_c}{2m_0}\right)^{1/2}[i(E_x e^{i\omega t} - \text{c.c})\sqrt{\alpha_1}(a^\dagger - a) - (E_y e^{i\omega t} - \text{c.c})\sqrt{\alpha_2}(a^\dagger + a)]\right.$$

$$\left. - (E_z e^{i\omega t} - \text{c.c})\frac{\alpha_4}{\sqrt{\alpha_2}}(a^\dagger + a) + (E_z e^{i\omega t} - \text{c.c})\alpha_3\frac{P_z}{m_0}\right], \tag{A1}$$

$$\mathcal{H}_2' = \frac{1}{2}\frac{e}{i\omega}\frac{i}{\hbar}[\mathcal{H}_2, \vec{r}\,][(E_x e^{i\omega t} - \text{c.c.})\hat{x} + (E_y e^{i\omega t} - \text{c.c.})\hat{y} + (E_z e^{i\omega t} - \text{c.c.})\hat{x}], \tag{A2}$$

$$M^{C1}(s) \equiv M_1^{C1}(s) + M_2^{C1}(s), \tag{A3}$$

$$M_1^{C1}(s) = \langle\overline{\rho'}|\mathcal{H}_1'|\rho\rangle, \tag{A4}$$

$$M_2^{C2}(s) = \langle\rho'|\mathcal{H}_1'|\rho\rangle, \tag{A5}$$

where ρ' and ρ are $(n+1,\ k_z,\ k_y,\ s)$ and $(n,\ k_z,\ k_y,\ s)$, respectively, and $|\overline{\ }\rangle$ means the state corresponding to the wave function with first-order corrections [Eq. (11)].

Neglecting E_z we get[41]

$$M_1^{C1}(s) = \frac{1}{2}\frac{ei}{\omega}\left(\frac{\hbar\omega_c}{2m_0}\right)^{1/2}(n+1)^{1/2}[iE_x^*\sqrt{\alpha_1}(1+\tfrac{1}{2}W) - E_y^*\sqrt{\alpha_2}(1-\tfrac{1}{2}W)], \tag{A6}$$

$$W = \{A[\cos^4\phi - (\alpha_2/\alpha_1)^2] + 2B\cos^2\phi\sin2\phi + \tfrac{3}{2}C\sin^2 2\phi + D\sin^4\phi\}\frac{3\hbar\omega_c}{\alpha_2^2}(n+1) + \frac{\mathcal{G}_{xx}^s}{\alpha_1} - \frac{\mathcal{G}_{yy}^s}{\alpha_2}$$

$$+\left[A\frac{3u^2\cos^2\phi}{\alpha_2} - \frac{u}{\alpha_1} - 6Bu\left(\frac{v}{\alpha_1} + \frac{\cos\phi}{\alpha_2}(v - u\sin\phi)\right) + 3C[(v^2\cos^2\phi + u^2\sin^2\phi - 2uv\sin2\phi)/\alpha_2 - v^2/\alpha_1]\right]\frac{2p_z^2}{m_0}, \tag{A7}$$

$$M_2^{C1}(s) = \frac{1}{2}\frac{ei}{\omega}\left(\frac{\hbar\omega_c}{2m_0}\right)^{1/2}(n+1)^{1/2}\ 12iE_x^*\left(\left[A\left(\frac{1}{\alpha_1} + \frac{\cos^2\phi}{3\alpha_2}\right) - \frac{B}{\alpha_2}\sin2\phi + C\frac{\sin^2\phi}{\alpha_2}\right]\frac{\hbar\omega_c}{2}(n+1)\right.$$

$$+\left\{\frac{A}{3}\left[\cos^2\phi\left(\frac{\alpha_4}{\alpha_2}\right)^2 + \sin^2\phi\right] + B\sin2\phi\left[1 - \left(\frac{\alpha_4}{\alpha_2}\right)^2\right] + C\left[\cos^2\phi + \left(\frac{\alpha_4}{\alpha_2}\right)^2\sin^2\phi\right]\right\}\frac{p_z^2}{m_0} + 2\mathcal{G}_{xx}^s\Big)$$

$$- E_y^*\left[\left(\frac{3}{\alpha_2}[2(A\cos^4\phi + D\sin^4\phi) + 4B\cos^2\phi\sin2\phi + 3C\sin^2 2\phi] + \frac{2}{\alpha_1}(A\cos^2\phi - 3B\sin2\phi + 3C\sin^2\phi)\right)\right.$$

$$\times\hbar\omega_c(n+1) + \{A[12(\alpha_4/\alpha_2)^2\cos^4\phi + 3\sin^2 2\phi - 6(\alpha_4/\alpha_2)^2\cos\phi\sin2\phi]$$

$$+ B[24(\alpha_4/\alpha_2)^2\cos^2\phi\sin2\phi + 12(\alpha_4/\alpha_2)\cos^2\phi(1 - 4\sin2\phi) - 12\sin2\phi\cos2\phi]$$

$$+ C[18(\alpha_4/\alpha_2)^2\sin^2 2\phi + 18(\alpha_4/\alpha_2)\sin2\phi\cos2\phi + 12(1 - \tfrac{3}{2}\sin^2 2\phi)] + D[12(\alpha_4/\alpha_2)^2$$

$$\left. + 3\sin^2 2\phi + 6(\alpha_4/\alpha_2)\sin^2\phi\sin2\phi]\right\}\frac{p_z^2}{m_0} + 2\mathcal{G}_{yy}^s\Big]. \tag{A8}$$

B. Second- and third-harmonic cyclotron resonances

For these transitions we have only considered $\theta = 0°$, and for the third harmonic the contribution from the spin-dependent part of the Hamiltonian and the z component of the electric field has been neglected. Thus, these results are only for the purpose of obtaining order-of-magnitude estimates for the intensity of these transitions for the case H parallel to the bisectrix axis or close to this condition.

2nd-harmonic cyclotron resonance:

$$M^{C2} = \frac{1}{2}\frac{ei}{\omega}B\frac{p_z}{m_0}[(n+1)(n+2)]^{1/2}12\hbar\omega_c\frac{iE_X^*}{(\alpha_1\alpha_2)^{1/2}}. \tag{A9}$$

3rd-harmonic cyclotron resonance:

$$M^{C3} = \frac{1}{2}\frac{ei}{\omega}\left(\frac{\hbar\omega_c}{2m_0}\right)^{1/2}[(n+1)(n+2)(n+3)]^{1/2}\frac{\hbar\omega_c}{2}$$

$$\times\left(\frac{iE_X^*}{(\alpha_1)^{1/2}}\frac{15C}{\alpha_2} - \frac{7}{2}\frac{A}{\alpha_1} - \frac{3}{2}\frac{D\alpha_1}{\alpha_2^2}\right.$$

$$\left. + \frac{E_Y^*}{(\alpha_2)^{1/2}}\frac{15C}{\alpha_1} - \frac{7}{2}\frac{D}{\alpha_2} - \frac{3}{2}\frac{A\alpha_2}{\alpha_1^2}\right). \tag{A10}$$

C. Spin-flip resonance

$$M^{SF}=\frac{1}{2}\frac{ei}{\omega}\frac{p_z}{m_0}\left\{iE_x^*\left[\sqrt{\alpha_1}\,(W-Z)+2i\left(T_{xy}\frac{\alpha_4}{\alpha_2}-T_{xz}\right)\right]-E_y^*\left[\sqrt{\alpha_2}\,(W+Z)-2i\left(T_{yy}\frac{\alpha_4}{\alpha_2}-T_{yz}\right)\right]-E_z^*\frac{\alpha_4}{\alpha_2}(W+Z)\right\}, \tag{A11a}$$

$$W=(T_B-T_A)/(1-\gamma)\,, \tag{A11b}$$

$$Z=(T_A+T_B)/(1+\gamma)\,, \tag{A11c}$$

$$T_A=[T_{xy}(\alpha_4/\alpha_2)-Y_{xz}]/\sqrt{\alpha_1}\,, \tag{A11d}$$

$$T_B=[T_{yy}(\alpha_4/\alpha_2)-T_{yz}]/\sqrt{\alpha_2}\,, \tag{A11e}$$

$$T_{ij}=\sum_{\mu\nu}\tau_\mu H_\nu G_{\mu\nu,ij}\,, \tag{A12}$$

$$\tau_\mu=\langle -1\,|\,\sigma_\mu\,|+1\rangle\,, \tag{A13}$$

$$\tau_1=ib\,,\quad \tau_2=-ia\,,\quad \tau_3=-1\,. \tag{A14}$$

D. Combined resonance

$$M^{CO1,2}=\frac{1}{2}\frac{ei}{\omega}\left(\frac{\hbar\omega_c}{2m_0}\right)^{1/2}(n+1)^{1/2}\left\{iE_x^*\left[\sqrt{\alpha_1}\,(W-Z_{1,2})-2\left(\pm\frac{T_{xx}}{(\alpha_1)^{1/2}}-\frac{iT_{xy}}{(\alpha_2)^{1/2}}\right)\right]\right.$$
$$\left.-iE_y^*\left[\sqrt{\alpha_2}\,(W+Z_{1,2})-2\left(\pm\frac{T_{yy}}{(\alpha_2)^{1/2}}+\frac{iT_{xy}}{(\alpha_1)^{1/2}}\right)\right]-E_z^*\left[\frac{\alpha_4}{(\alpha_2)^{1/2}}(W+Z_{1,2})-2\left(\mp\frac{T_{yz}}{(\alpha_2)^{1/2}}+i\frac{T_{xz}}{(\alpha_1)^{1/2}}\right)\right]\right\}\,, \tag{A15}$$

$$M^{CO3}=\frac{1}{2}\frac{ei}{\omega}\left(\frac{\hbar\omega_c}{2m_0}\right)^{1/2}(n+1)^{1/2}iE_x^*\left(\sqrt{\alpha_1}\,(W_3-Z_3)+2\frac{T_{xx}}{(\alpha_1)^{1/2}}+i\frac{T_{xy}}{(\alpha_2)^{1/2}}\right)$$
$$-E_y^*\left(\sqrt{\alpha_2}(W_3+Z_3)-2\frac{T_{yy}}{(\alpha_2)^{1/2}}-i\frac{T_{xy}}{(\alpha_1)^{1/2}}\right)-E_z^*\left(\frac{\alpha_4}{(\alpha_2)^{1/2}}(W_3+Z_3)-2\frac{T_{yz}}{(\alpha_2)^{1/2}}-i\frac{T_{xz}}{(\alpha_2)^{1/2}}\right)\,. \tag{A16}$$

In the above expression we have

$$W=-(1/\gamma)(T_{xx}/\alpha_1+T_{yy}/\alpha_2)\,, \tag{A17}$$

$$Z_{1,2}=\pm\frac{1}{2\pm\gamma}\left(-\frac{T_{xx}}{\alpha_1}+\frac{T_{yy}}{\alpha_2}\pm i2\frac{T_{xy}}{(\alpha_1\alpha_2)^{1/2}}\right)\,, \tag{A18}$$

$$W_3=-Z_2\,,\qquad Z_3=-W\,. \tag{A19}$$

---

*Research supported by the NSF under Grant No. 40968.
†The computer time for this work was supported in full through the facilities of the Computer Science Center of the University of Maryland.
‡On leave of absence from the Dep. of Physics, Universidad Nacional de Ingenieria, Lima, Peru.
§ Present address: Universidad Nacional de Ingenieria, Departamento de Fisica, Casilla de Correo 1301, Lima, Peru.

[1]R. T. Bate and N. G. Einspruch, Phys. Rev. 153, 796 (1967); R. T. Bate and N. G. Einspruch, *Proceedings of the International Conference on the Physics of Semi-Metals of Sem., Kyoto*, 1966, J. Phys. Soc. Jpn. Suppl. 21, 673 (1966).
[2]R. T. Isaacson and G. A. Williams, Phys. Rev. 185, 682 (1969).
[3]L. A. Fal'kovskii, Usp. Fiz. Nauk. 94, 3 (1968) [Sov. Phys.-Usp. 11, 1 (1968)]; M.S. Dresselhaus, *The Physics of Semimetals and Narrow-Gap Semiconductors* edited by D. L. Carter and R. T. Bate (Pergamon, New York, 1971).
[4](a) R. Blewitt and A. J. Sievers, Phys. Rev. Lett. 30, 1041 (1973); (b) R. L. Blewitt and A. J. Sievers, J. Low Temp. Phys. 13, 617 (1973).
[5]S. Golin, Phys. Rev. 166, 643 (1968).
[6]H. R. Verdún and H. D. Drew, Phys. Rev. Lett. 33, 1608 (1974).
[7]H. R. Verdun and H. D. Drew (unpublished).
[8]L. G. Ferreira, J. Phys. Chem. Solids 28, 1891 (1967); L. G. Ferreira, J. Phys. Chem. Solids 29, 357 (1968); there have been other calculations of the band structure of bismuth using the tight-binding approximation. See for example, S. Mase, J. Phys. Soc. Jpn. 13, 434 (1958) and 14, 584 (1959).
[9]S. H. Koenig, A. A. Lopez, D. B. Smith, and J. L. Yarnell, Phys. Rev. Lett. 20, 48 (1968).
[10]L. G. Ferreira (Ref. 8) also gives these matrix elements.
[11]Y. Yafet, *Solid State Physics*, edited by F. Seitz and D. Turnbull (Academic, New York, 1963), Vol. 14, p. 1.
[12]H. J. Zeiger and G. W. Pratt, *Magnetic Interactions in Solids* (Clarendon, Oxford, 1973).

[13]R. T. Bate, N. G. Einspruch, and P. J. May, Jr., Phys. Rev. 186, 599 (1969).
[14]R. L. Bell and K. T. Rogers, Phys. Rev. 152, 746 (1966).
[15]We are also neglecting the normalization corrections introduced by our perturbational approach to the calculation of the envelope functions.
[16]E. I. Rashba and V. I. Sheka, Fiz. Tverd, Tela 3, 1735 (1961) [Sov. Phys.-Solid State 3, 1257 (1961)].
[17]P. A. Wolff, J. Phys. Chem. Solids 25, 1057 (1964).
[18]H. D. Drew, University of Maryland Technical Report No. 921 (1969).
[19]R. J. Wagner and G. A. Prinz, Appl. Opt. 10, 2060 (1971); R. J. Wagner, A. J. Zelano, and L. H. Ngai, Opt. Commun. 8, 46 (1973).
[20]W. G. Pfann, *Zone Melting*, 2nd ed. (Wiley, New York, 1966). J. H. Wernick, K. E. Benson, and D. Dorsi, AIME Trans. 209, 966 (1957).
[21]U. Strom, Ph.D. thesis, (University of Maryland, 1972) (unpublished). See also Ref. 4b.
[22]A. N. Friedman, Phys. Rev. 159, 553 (1967).
[23]G. E. Smith, G. A. Baraff, and J. M. Rowell, Phys. Rev. 135, A1118 (1964).
[24]B. McCombe and G. Siedel, Phys. Rev. 155, 633 (1967).
[25]T. Sakai, Y. Matsumoto, and S. Mase, J. Phys. Soc. Jpn. 27, 862 (1969).
[26]V. S. Édel'man, Zh. Eksp. Teor. Fiz. 64, 1734 (1973) [Sov. Phys.-JETP 37, 875 (1973)].
[27]T. L. Cronburg and B. Lax, Phys. Lett. A 37, 135 (1971).
[28]See, for example, this recent review B. D. McCombe and R. J. Wagner, *Advance in Electronics and Electron Physics*, Vol. 38 (Academic, New York, to be published).
[29]A. M. Kosevich and L. V. Tanatarov, Fiz. Tverd. Tela 6, 3423 (1964) [Sov. Phys.-Solid State 6, 2738 (1965)]; É. A. Kaner and É. P. Feldman, Zh. Eksp. Teor. Fiz. 58, 1803 (1970) [Sov. Phys.-JETP 31, 966 (1970)]; M. V. Ortenberg, Phys. Status Solidi 60, 273 (1973).
[30]G. A. Williams and E. A. Smith, IBM J. Res. Dev. 8, 276 (1964) See also Ref. 2.
[31]S. Takano and H. Kawamura, J. Phys. Soc. Jpn. 28, 348 (1970).
[32]P. M. Platzman and P. A. Wolff, *Waves, and Interactions in Solid State Plasmas* (Academic, New York 1973); E. A. Kaner and V. G. Skobov, *Electromagnetic Waves in Metals in a Magnetic Field* (Taylor and Francis, London, 1968).
[33]See Ref. 39 and references therein.
[34]G. E. Smith, L. C. Hebel, and S. J. Buchsbaum, Phys. Rev. 129, 154 (1963).
[35]T. Akahane and Y. Uemura, J. Phys. Soc. Jpn. 31, 990 (1971).
[36]J. Nakahara, H. Kawamura, and Y. Sawada, Phys. Rev. B 3, 3155 (1971).
[37]V. P. Naberezhnikh, D. E. Zherebchevskii, and V. L. Mel'nik, Zh. Eksp. Teor. Fiz. 63, 169 (1972) [Sov. Phys.-JETP 36, 89 (1973)].
[38]We used the experimental results obtained in Faraday configuration instead of the more complete set of data obtained in Voigt configuration to compare with the theoretical predictions because we think that the characterization of the propagating modes using the local approximation is much better for the Faraday configuration.
[39]M. Weiler, B. Lax, W. Dreybrodt, and K. J. Button, *Proceedings of the Tenth International Conference on the Physics of Semiconductors, Cambridge, Massachusetts*, 1970, edited by S. P. Keller, J. C. Hansel, and F. Stern (USAEC, Division of Technical Information, 1970, or National Information Service, NBS Conf. -700801), p. 847.
[40]See Fig. 3 for the definition of these transitions.
[41]W. S. Benedict, M. A. Pollack, and W. J. Tomlinson, III, IEEE J. Quantum Electron. 5, 108 (1969).
[42]L. C. Robinson, *Physical Principles of Far-Infrared Radiation* (Academic, New York, 1973).
[43]R. J. Dinger and A. W. Lawson, Phys. Rev. B 7, 5215 (1973).
[44]M. P. Vecchi and M. S. Dresselhaus, Phys. Rev. B 9, 3257 (1974).
[45]V. S. Édel'man and M. S. Khaikin, Zh. Eksp. Teor. Fiz. 49, 107 (1965) [Sov. Phys.-JETP 22, 77 (1966)].